Materials & Design 213 (2022) 110300

Contents lists available at ScienceDirect

Materials & Design

journal homepage: www.elsevier.com/locate/matdes

Probabilistic analysis of additively manufactured polymer lattice structures

Sven Drücker [a], Julian Kajo Lüdeker [b], Marvin Blecken [c], Arne Kurt [a], Kirill Betz [a], Benedikt Kriegesmann [b], Bodo Fiedler [a]

[a] Hamburg University of Technology, Institute of Polymers and Composites, Denickestr. 15, 21073 Hamburg, Germany
[b] Hamburg University of Technology, Working Group Structural Optimization for Lightweight Design, Am Schwarzenberg-Campus 4, 21073 Hamburg, Germany
[c] Hamburg University of Technology, Institute of Aircraft Cabin Systems, Hein-Saß-Weg 22, 21129 Hamburg, Germany

HIGHLIGHTS

- Probabilistic influence of geometry and material properties in lattice structures are captured in finite element simulations.
- A new probabilistic model for strength and fracture strain distribution is proposed.
- Variograms of 3D digital image correlation are used for correlation length determination.
- Probabilistic methods are valuable for robust design with lattice structures.

GRAPHICAL ABSTRACT

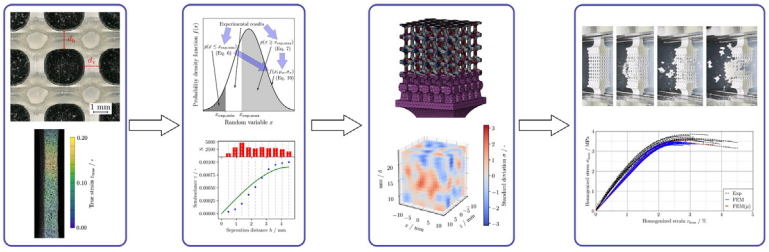

ARTICLE INFO

Article history:
Received 18 June 2021
Revised 26 October 2021
Accepted 4 December 2021
Available online 7 December 2021

Keywords:
Finite Element Method
3D Printing
Stereolithography
Progressive Damage
Stochastic Modeling
Strength Variation

ABSTRACT

Filigree lattice structures are sensible to geometrical imperfections and the scatter of material parameters which all depend on the stability of the manufacturing process. The aim of this study is to analyze these effects for polymer lattice structures and incorporate them in a finite element model for robust design. Micrographs of lattice structure slices show a smaller diameter for vertical struts. Basic mechanical tests on bulk material exhibit a tension–compression asymmetry which is captured with a Drucker-Prager material model in simulations. Digital image correlation measurements allow to determine true material properties. Plateau stress and failure strain are a result of the biggest flaw in the specimen. Hence, a new model to determine their probability distribution is proposed. This model outperforms standard approaches deriving the probability distribution from the central moments. A spatial correlation of geometric deviations and scatter of the material is investigated with variography subsequently allowing to model the varying properties with random fields. Simulations of dog-bone specimens show that the probability distributions of material properties are captured well. Also simulations of lattice structures are able to represent the probability distributions of their homogenized mechanical properties. The whole stress–strain response and the failure progression agree well with experimental results.

1. Introduction

Although cellular structures have already been explored in the past [1–3], the progress in additive manufacturing over the past decade has further enhanced the excitement, as many manufacturing restrictions are abolished. The combination of mathematics and manufacturing is particularly powerful where two disciplines, topology optimization and additive manufacturing, profit from

https://doi.org/10.1016/j.matdes.2021.110300
0264-1275/

each other [4,5]. One of the few remaining constraints is the resolution of the prints where filigree cellular structures push the limit. Tailoring unit cells according to the specified requirements by topology optimization takes full advantage of additive manufacturing [6]. Lattice structures consisting of many unit cells can be seen as metamaterials and are attractive to many disciplines such as heat conduction [7–9], medical engineering [10,11], chemical reactors [12–14] or structural design [15] to mention a few.

Lightweight design has become increasingly important, as it leads to energy savings in the transport sector and thus has ecological as well as economic benefits. For lightweight structural applications Ashby [16] suggests stretch-dominated cellular materials because of their higher stiffness and initial collapse strength. Sigmund [17] reported that closed-wall unit cells perform best with regard to stiffness under triaxial loading, however, these are not suited for many 3D printing applications as material can get entrapped. The surplus material does not support the mechanical behavior but increases weight. Hence, it is not favorable in lightweight design. This is valid for all processes with a powder bed (for instance selective laser sintering and melting) or a resin bath (for example stereolithography (SLA)) which are three of the four major techniques in additive manufacturing. An optimized open-wall unit cell with regard to stiffness under triaxial loading is composed of struts along the edges of a cube and thus called "cubic" [17,18]. In addition, a non-uniform parameterization of the individual struts is possible leading to an anisotropic unit cell and shows improvements with regard to compliance minimization [19]. The cubic unit cell is therefore analyzed in this study. We focus on tensile tests of lattice structures as they are rather rare in the literature so far [20] and equally important for lightweight structural applications. The lattice structures are manufactured in an SLA process with a photopolymer resin.

Further insights into the deformation behavior of lattice structures can be gained by the finite element method (FEM) which allows a higher temporal and local resolution of the stresses and strains. In a straightforward manner different unit cells were investigated with respect to stress concentrations using linear-elastic material models [21–24]. The nonlinear material behavior of lattice structures has been reproduced in several studies with elastoplastic models using different definitions of the plastic flow such as von Mises [25–28], Johnson–Cook [29], Gurson-Tvergaard-Needleman [30] or Hill [31]. The progressive damage was accounted for by some researchers [32,30,33]. So far, a tension–compression asymmetry was not considered in the plasticity models for lattice structures despite the fact that additive manufacturing is prone to imperfections such as pores which are dependent on the process parameters [34]. These pores are more severe under tensile loading due to higher stress concentrations resulting in earlier failure [35]. This is even more critical for polymer materials where the strength differential is naturally inherent even without defects. This might explain the differences in the plastic regime of experiments and simulations Ling et al. [27] found, as they calibrated the material model with bulk tensile tests and used it in compressive lattice simulations. To account for the tension–compression asymmetry, we use a Drucker-Prager yield surface in this study.

In filigree lattice structures imperfections leave uncertainties in the design especially when the limits are pushed to small volume fractions. The traditional approach of using safety factors is not desirable in structural lightweight design. Two competing aims need to be satisfied: (i) the safety factor has to be as high as possible to be sure that the structures can withstand the load and (ii) the safety factor should be as small as possible to save weight. As safety factors only depend on past experience, this leaves engineers with a dilemma. In such cases, probabilistic analysis is an approach for more rational decisions [36]. The stochastic FEM is one of the methods frequently used in the past [37]. In this study, we use the Monte-Carlo simulation framework, where several realizations of the design with random stochastic varying input parameters are analyzed in terms of their varying resulting performance. Generally the stochastic variation of material properties, geometry and loads can be analyzed [38]. Kriegesmann et al. [39] successfully applied probabilistic methods on structures with geometric and loading imperfections. Also for lattice structures stochastic effects have been analyzed for a shape optimized unit cell [40]. On the structural level, only few investigations regarding geometry imperfections and varying material properties allowed a comparison of simulated with experimentally observed stochastic distributions[41,42]. In order to incorporate stochastic variations of the geometry in the model, different approaches can be found in the literature. Scanning electron microscopy (SEM) images were analyzed and imperfections of the struts were represented in models by stacked beams with different cross-section diameters [43] or by stacked intersecting spheres [44]. In other studies computed tomography (CT) scans of cellular materials were captured and then directly used as models [45,26]. As this is usually computationally expensive, Lozanovski et al. [28] developed a modeling approach with elliptical cross-sections joined by a loft operation. Input parameters were gathered from slices of CT images and then applied on the model for individual struts and complete lattices. They also determined varying effective strut properties and applied them on straight beam elements in full lattice models [46]. Moreover, geometrical imperfections were modelled by introducing buckling eigenmodes [47]. With regard to material property variations different implementations were found. For honeycomb structures the elastic modulus was varied together with the sheet thickness based on assumed coefficients of variation [48]. Furthermore, a stochastic approach for the elastic properties as well as the geometry was used for foams [49]. In this case a spatial correlation was analyzed and applied with random fields. Yet, studies capturing variations in the nonlinear part of the material model (plasticity and failure) are rather rare even outside the field of cellular materials. Ning et al. [50] implemented a probabilistic FEM for elastoplastic materials but did not validate it with experiments. Amani et al. [30] used the porosity gained from CT scans to vary the plastic material properties of their Gurson-Tvergaard-Needleman model which needs the porosity as an input. However, they only directly transferred the CT data to the FEM model in one deterministic case without considering several realizations to capture the scatter. Clouston and Lam [51] worked on strand-based wood composites and captured the variation in plastic properties. They included a size effect for the strength when evaluating different specimen volumes. Good results were obtained in validations with experiments in different loading cases. Yet, including the size effect in the probability distributions of the plastic properties adds geometric influences to the material, making it impossible to distinguish the individual effects. This shows the challenge in probabilistic analysis of material properties that are governed by localization phenomena like plasticity. However, modeling these phenomena is crucial for a robust design. The linear elastic regime can be considered relatively safe anyway, but especially the nonlinear behavior afterwards needs to be analyzed. Hence, the aim of this work is to implement a probabilistic analysis capturing geometrical imperfections as well as variations of the material properties also beyond the linear elastic limit. A new model is proposed on how to determine the probability distribution of local properties like strength and fracture strain.

This study is comprehensive and structured as follows. In Section 2 the utilized materials and methods are introduced. The sample preparation is explained and subsequently a description of quality control, geometry and material characterization is given.

Afterwards, variography and a new model to determine the probability distributions of material properties governed by local phenomena are presented. These are used in the following for the stochastic variations in the FEM modeling. The results are presented and discussed in Section 3, starting with the quality control of the post-curing, geometrical deviations and material properties. Correlation length and probability distributions of the parameters with variography and the newly proposed model are shown. A verification of the material model as well as validations of the material property and geometry deviation distributions are carried out by a comparison of FEM simulations with experiments. Conclusions are drawn in Section 4.

2. Materials and methods

In this section, the sample preparation is described with a quality control of curing by differential scanning calorimetry (DSC). The characterization of the geometry and the mechanical testing procedure are presented. The use of variography to generate parameters for random fields of varying specimen properties is explained and a model is proposed to estimate the stochastic distribution of local mechanical properties. Finally, the FEM model is introduced.

2.1. Sample preparation

To analyse the stochastic variation of dimensional accuracy and the mechanical properties, specimens are manufactured in an SLA process with a 3D printer (Form 2, Formlabs Inc., Somerville, MA, USA) and a photopolymer resin (Clear, Formlabs Inc., Somerville, MA, USA). After printing, excess resin is removed in an isopropanol bath. Post-curing is performed in an ultraviolet (UV) radiation oven (Form Cure, Formlabs Inc., Somerville, MA, USA) at 60 °C for 4 h. Afterwards, support structures are removed and the contact points are polished with sandpaper. To characterize the material properties, three different specimens are analyzed. Tensile properties are evaluated with dog-bone specimens of type 1BB with a thickness of 3 mm according to DIN EN ISO 527–2 [52]. Compressive tests are performed with rectangular block specimens of type B after DIN EN ISO 604 [53]. The critical strain energy release rate is investigated with single-edge-notch bending (SENB) specimens with dimensions of 40 mm × 8 mm × 4 mm in agreement with ASTM D5045 [54]. A notch of 4 mm is introduced by a precision saw (Brillant 220, ATM Qness GmbH, Mammelzen, Germany) with a 150 μm diamond cut-off wheel followed by initiating the natural crack with a razor blade in a sawing motion. All specimens for the material characterization are printed with a layer height of 100 μm.

The unit cell of the cubic lattice consists of three orthogonal struts with a diameter of 1.1 mm. Fillets are added to reduce stress concentrations as shown in Fig. 1a. The unit cell has a dimension of 4 mm × 4 mm × 4 mm, yielding a volume fraction of approximately 20 %. The unit cells are periodically repeated 5 × 5 times over the cross-section and 6 times over the length to form the lattice structure specimens. The unit cell repetitions are chosen in such a way that the influence of a size effect is small. According to Andrews et al. [55], the size effect vanishes with a ratio of 5 to 8 of the specimen size to the unit cell size, depending on whether a closed or open cell foam is considered and whether the stiffness or the strength is analyzed. In contrast to foams, the lattice structures in this study are periodic so the results might not be perfectly transferable. To reduce computational time in the numerical model, a ratio of 5 is chosen for the cross-section. In order to allow an oblique fracture, a length of 6 unit cells is chosen. The load introduction is realized by a clamping area connected to a base plate with a fillet. In addition, two rows of cells with a gradient in volume fraction are added in between to reduce the stiffness jump from the bulk clamping area to the lattice structure preventing early failure [56,35]. The gradient in volume fraction is realized by an increasing strut diameter towards the base plate. The morphological characteristics of the unit cells with a gradient and in the middle section of the lattice structure specimens, as specified in computer aided design (CAD), are summarized in Table 1. The diameter of the lower strut d_l towards the base plate, the diameter of the upper strut d_u towards the unit cells in the middle section, the diameter of the horizontal struts d_h, the fillet radius r_f and the resulting volume fraction V_f are given. The lattice structure specimen with the gradient in volume fraction at the load introduction is presented in Fig. 1b. As the lattice geometry is more complex, a higher resolution of the layer height with 25 μm is used. Preliminary experiments with different layer thicknesses only showed minor differences that were within the reproducibility of the printing process of such a low-cost SLA printer. The lattice structure specimens are built as indicated in Fig. 1b, so that building direction and loading direction coincide. Finally, the material characterization and lattice specimens with their dimensions in mm are summarized in Fig. 2.

2.2. Differential scanning calorimetry

Zguris [57] suggests post-curing at 60 °C for 1 h in a UV oven. However, it remains unclear why this conclusion is drawn as the strength of the material still increases for curing longer than 1 h. An own preliminary study showed that stiffness and strength reach a plateau after approximately 4 h. For quality control of the curing degree of the specimens, a thermal analysis is performed by DSC (DSC 204 F1 Phoenix, NETZSCH-Gerätebau GmbH, Selb, Germany). An exemplary sample of approximately 15 mg is cut from the specimens and analyzed from −20 °C to 230 °C with a rate of 20 K min^{-1} under nitrogen atmosphere. A dog-bone specimen is tested (i) as printed without post-curing, (ii) post-cured only in the oven at 60 °C for 2 h and (iii) post-cured only by UV radiation for 2 h as references to investigate the different influences of the the curing mechanisms. Moreover, a dog-bone specimen (iv) and a lattice structure (v) both post-cured in a UV oven at 60 °C for 4 h are examined. Incomplete curing is visible by residual reaction enthalpy occurring during heating the sample.

2.3. Geometry characterization

Regarding the mechanical properties of the lattice structures, the smallest diameter of the struts in loading direction is crucial. Furthermore, also the diameter of horizontal struts is important for the transverse contraction behavior. Thus, the dimensional accuracy of the struts is explored with digital microscopy (VHX-6000, Keyence Deutschland GmbH, Neu-Isenburg, Germany). To also get an insight in the strut dimensions in the inner part of the lattice, the load introduction is removed and the remaining lattice is sliced in five parts by a precision saw (Brillant 220, ATM Qness GmbH, Mammelzen, Germany) as depicted in Fig. 3. A micrograph of each slice is taken and the vertical d_v and horizontal diameters d_h of the struts are evaluated. A total of six specimens is analyzed yielding 150 vertical and 144 horizontal strut diameter measurements.

2.4. Mechanical testing

In order to determine the variation in the material properties, uniaxial tensile tests according to DIN EN ISO 527–1 [58] are performed on a universal testing machine (Z2.5, ZwickRoell GmbH & Co. KG, Ulm, Germany) with a crosshead speed of 0.25 mm min^{-1}. Here, 9 specimens are tested and clamped by screw grips. As poly-

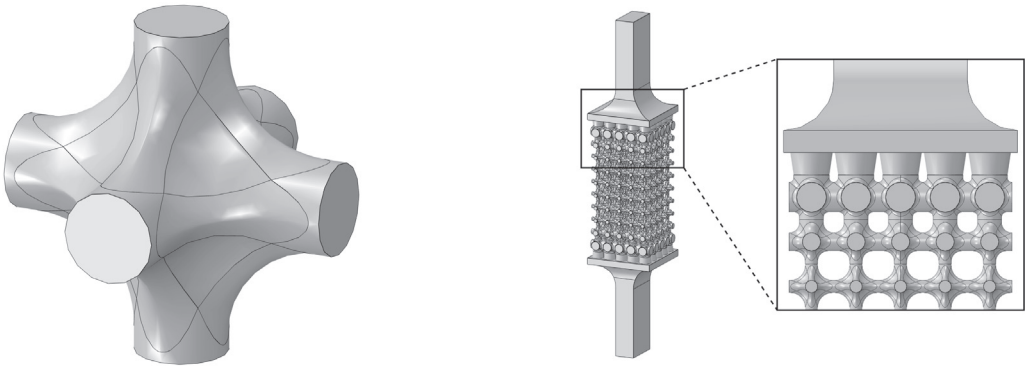

(a) Cubic unit cell with 20 % volume fraction.

(b) Lattice structure specimen with gradient at load introduction.

Fig. 1. Cubic unit cell (a) and lattice structure specimens for tensile testing (b) with gradient in volume fraction at the load introduction of the tensile specimens.

Table 1
Morphological characteristics of the unit cells as specified in CAD.

Unit cell	d_l / mm	d_u / mm	d_h / mm	r_f / mm	V_f / %
1st gradient	3.2	2.15	2.68	0.39	65
2nd gradient	2.15	1.1	1.63	0.91	33
Middle section	1.1	1.1	1.1	1.32	20

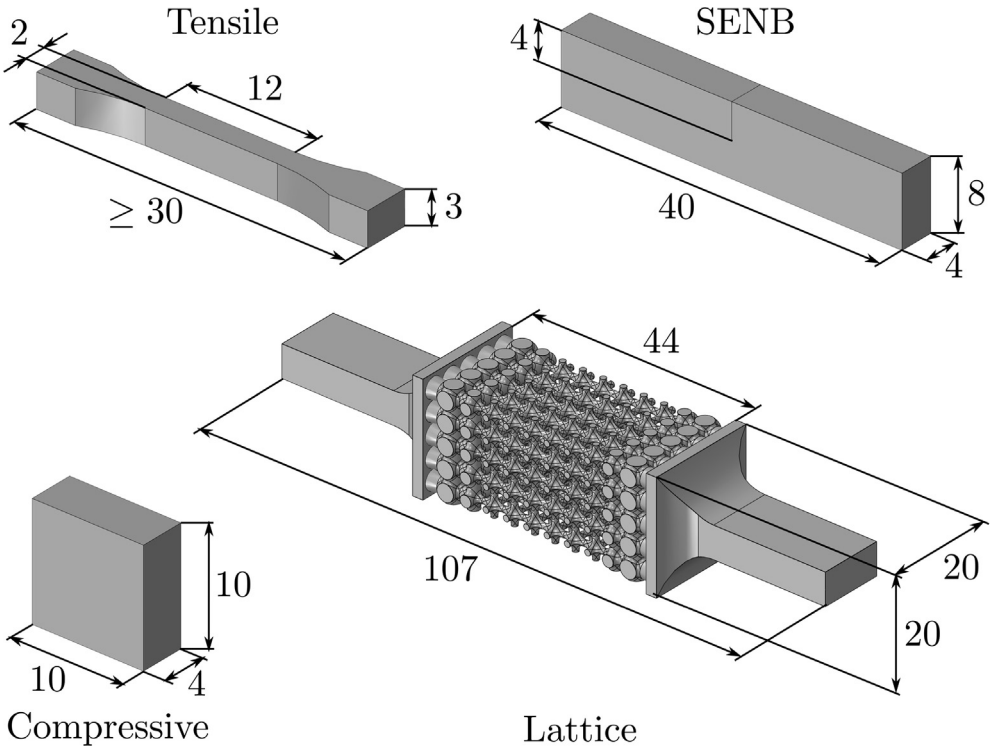

Fig. 2. Types of specimens used for material characterization and lattice structure specimens with their dimensions in mm: tensile test (upper left), SENB test (upper right), compressive test (lower left), lattice structure tested in tension (lower right).

mers often show a tension–compression asymmetry [59], also uniaxial compressive tests conforming with DIN EN ISO 604 [53] are executed. A universal testing machine (Z010, ZwickRoell GmbH & Co. KG, Ulm, Germany) with a crosshead speed of 1 mm min^{-1} is utilized to evaluate 15 specimens. Polypropylene films are placed between the dies and specimens to avoid bulging due to friction during the experiment. The critical strain energy release rate can be used to capture progressive damage. Therefore, SENB tests in agreement with ASTM D5045 [54] are conducted on the universal testing machine (Z2.5, ZwickRoell GmbH & Co. KG, Ulm, Germany) where the specimens are supported by rollers with a diameter of 6 mm and a spacing of 32 mm. A crosshead speed of 10 mm min^{-1}

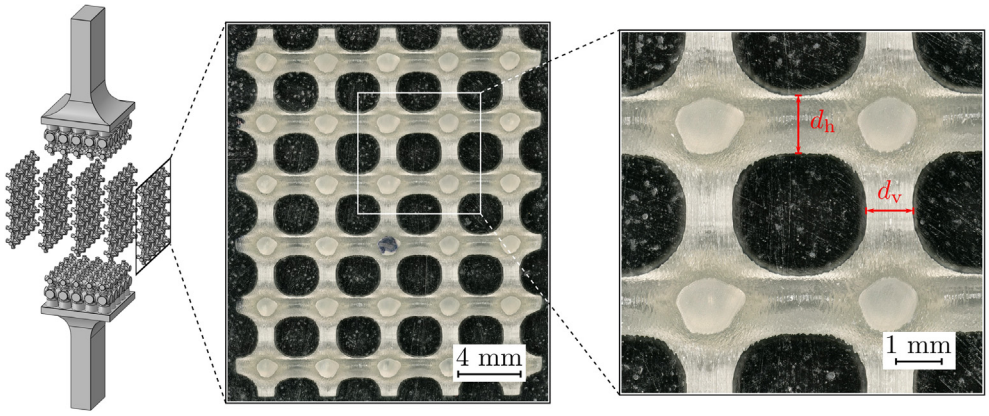

Fig. 3. Cutting of the lattice structure specimens and micrograph analysis for the geometry characterization by strut diameter measurements. The diameter of vertical struts d_v in loading direction and horizontal struts d_h perpendicular to it are highlighted.

is used to test 10 specimens. In order to determine the initial crack length, the fracture surface of the SENB specimens is captured by light optical microscopy (BX51, Olympus Deutschland GmbH, Hamburg, Germany) subsequent to the mechanical tests.

The mechanical characterization of the lattice structures is performed on a universal testing machine (Z2.5, ZwickRoell GmbH & Co. KG, Ulm, Germany) with a crosshead speed of 1 mm min^{-1} and a clamping with screw grips. The analysis consists of 19 specimens. As the performance of lattice structures is often evaluated against bulk material with regard to the weight savings, homogenized properties are desirable. The force F carried by a cross-section of the volume enclosing all unit cells A_0 is used to obtain the homogenized engineering stress σ_{hom} of the lattice structure specimens as depicted in Fig. 4a.

Strain measurements for the bulk tensile and compressive specimens characterizing material properties as well as for the lattice structure specimens are carried out with 3D digital image correlation (DIC) (Aramis 4 M, GOM GmbH, Braunschweig, Germany). The specimens are coated with white aerosol paint. A speckle pattern with black aerosol paint is applied after drying the first layer. DIC measurements allow to determine the engineering strain on the tensile and compressive bulk specimens by continuously tracking the distance change between two points, very similar to classical measurements with an extensometer. In that case, the initial measuring distance is chosen to 10 mm according to the standards DIN EN ISO 527–2 [52] and DIN EN ISO 604 [53]. Moreover, DIC measurements allow to evaluate the macroscopic homogenized strain of the lattice structures in a similar way without the influence of the load introduction geometry. Here, the homogenized engineering strain ε_{hom} is captured by continuously tracking the distance change ΔL between two points on the lattice cells in the middle part, with no gradient in volume fraction and an initial distance L_0 (see Fig. 4b). An even bigger advantage of DIC measurements is that they allow to measure the whole strain field. Hence, higher local strains at the necking of the tensile material characterization specimens and in the individual struts of the lattice structure specimens can be visualized. In case of the dog-bone specimens, the DIC software (Aramis 2016, GOM GmbH, Braunschweig, Germany) allows the evaluation at a single point of the true strain field. However, these single point measurements often show highly oscillating results, when facets are not recognized well. This is interpreted by the software as artificially large distortions. Instead, to determine the true strain of the dog-bone specimens, the change in distance L between two points in the necking region, with an initial distance L_0 of approximately 1 mm, is monitored. The initial distance is chosen in such a way, that the highest homogeneous strain in the necking is captured. The true strain ε_{true} is then calculated by integration with

$$\varepsilon_{true} = \int_{L_0}^{L} \frac{1}{L}\,\mathrm{d}L = \ln\left(\frac{L}{L_0}\right). \tag{1}$$

The transverse contraction in the necking area of the tensile material characterization specimens can be studied by DIC measurements without previously knowing its location. The transverse strain is recorded by the distance change between two points spanning the width of the specimen in the necking region. Assuming that the material is isotropic, this gives insights in the change in cross-sectional area and thus allows to determine the true stress.

2.5. Random fields and variography

The variation of properties such as geometry or material parameters is often spatially correlated. The properties at two different spatial points are usually more similar, the closer the points are. The reason for this is the manufacturing process. For instance, when there is shadowing in the post-curing process with the UV oven, then not only one tiny spot is affected, but also the regions around this spot see less curing energy due to partial shadowing. Hence, random fields are used to model a spatial correlation in the varying properties [60]. We assume a constant trend of the properties, a similar distribution at all spatial points and no directional dependence, thus a stationary, homogeneous and isotropic random field. Such a field for a property $\boldsymbol{x}$ can be generated from an uncorrelated random field by the inverse of the Mahalanobis transformation [61] with

$$\boldsymbol{x} = \boldsymbol{\Sigma}^{\frac{1}{2}}\boldsymbol{z} + \boldsymbol{\mu}_x, \tag{2}$$

where $\boldsymbol{z}$ is a vector of uncorrelated random numbers with zero mean and a standard deviation of one. The vector $\boldsymbol{\mu}_x$ contains the mean of x and $\boldsymbol{\Sigma}$ is the covariance matrix of x. Assuming a stationary random field with variance σ_x^2, the entries of the covariance matrix

$$\boldsymbol{\Sigma} = \boldsymbol{r}(\Delta\xi)\sigma_x^2 \tag{3}$$

can be calculated from the spatial autocorrelation function $\boldsymbol{r}$ depending on the distance of two points $\Delta\xi$. The square root of the covariance matrix can calculated via spectral decomposition

$$\boldsymbol{\Sigma}^{\frac{1}{2}} = \boldsymbol{Q}\boldsymbol{D}^{\frac{1}{2}}, \tag{4}$$

with $\boldsymbol{Q}$ being a matrix containing the eigenvectors of $\boldsymbol{\Sigma}$ and $\boldsymbol{D}$ being a diagonal matrix with the eigenvalues of $\boldsymbol{\Sigma}$ [41]. To save computational time, only eigenvalues that are at least a tenth of the largest

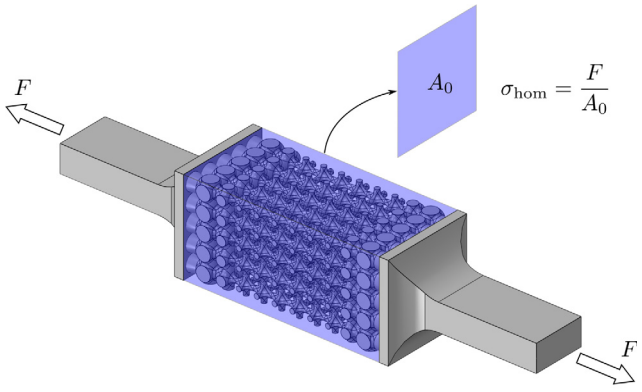

(a) Homogenized stress.

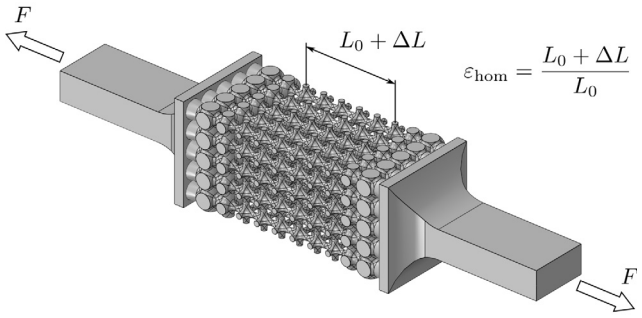

(b) Homogenized strain.

Fig. 4. Determination of the homogenized stress (a) and strain (b) for the lattice structures.

eigenvalue are considered. The procedure is also referred to as discrete Karhunen-Loève transform.

For determining the appropriate autocorrelation function, a method widely spread in geostatistics is used: variography [62]. A measure for the difference of the property x at two spatial points with a certain separation distance is given by the empirical Matheron semivariance

$$\gamma(h \pm \delta) = \frac{1}{2N(h \pm \delta)} \sum_{i,j \in N(h \pm \delta)} (x(\xi_i) - x(\xi_j))^2, \tag{5}$$

where h is the separation distance usually used as a discrete distance within a certain tolerance δ where measurements are grouped, N is the number of point pairs with separation distance h and ξ_i and ξ_j are spatial points [63]. Afterwards a mathematical function to describe the spatial relation is fitted through the variogram. For instance, the spherical model is given by

$$\gamma(h) = \begin{cases} c_0 + c\left(\frac{3h}{2r} - \frac{1}{2}\left(\frac{h}{r}\right)^3\right) & \text{for} 0 < h \leqslant r, \\ c_0 + c & \text{for} h > r, \end{cases} \tag{6}$$

with c_0 being the nugget, $c + c_0$ being the sill and r being the range. Since the sill is often not easy to recognize because it is reached asymptotically [64], we use the distance where 0.95 of the sill is reached as the correlation length l_c. Afterwards there is only a small increase in difference. To construct the variograms we use SCIKIT GSTAT [65].

2.6. Stochastic distribution of local mechanical properties

Determining the stochastic distribution of the mechanical properties is straightforward for quantities that are affected by the whole specimen such as the stiffness. They can be derived from the central moments and the histograms of the experimental results, which we call the "standard approach" in the following. However, for quantities that are dominated by local events like the true strength and local fracture strain, the standard approach is not sufficient. The experiment only shows the weakest part of the specimen or in other words the volume with the biggest flaw which was already found by Weibull [66]. Testing the remaining parts of the specimens for a second time would lead to a higher strength as the decisive defect in those sections of the specimen is smaller than in the initial specimen [67]. This also means, that the larger the tested volume, the weaker the experimental outcome as the probability to have a critical flaw is higher [68]. Assuming to have the distribution of the property from the sections with the biggest flaw over the whole specimen would lead to an artificially poor performance of the model. Hence, a new method is proposed to determine the stochastic distribution of these properties, which we call "local probability density function (PDF) model" hereafter. It is based on the assumption that the specimens consist of sections that have different properties depending on the flaws within them as depicted in Fig. 5a (the flaws are not considered directly but in a continuum mechanical sense as a homogeneous lower value of the property at that section). The basic idea is to find the probability p of the property x to be below $(x \leqslant x_{\text{exp,min}})$ and especially above $(x \geqslant x_{\text{exp,max}})$ the experimental results. Knowing these, a PDF $f(x)$ can be determined. The procedure is illustrated in Fig. 5b.

First, the part on the left-hand side of the experimental results in the probability density function is estimated. From all tested specimens with a specified number of sections only one has the minimal determined property or less. The probability p of a property x being below the lowest experimentally measured property $x_{\text{exp,min}}$ is determined by

$$p(x \leqslant x_{\text{exp,min}}) = \frac{1}{n_{\text{spec}} n_{\text{sec}}}, \tag{7}$$

where n_{spec} is the number of specimens tested and n_{sec} is the number of sections per specimen with homogeneous properties. To estimate the part on the right-hand side of the experimental results in the probability density function, a tree diagram helps to visualize the derivation (see Fig. 6). Only for one of the tested specimens all the sections are greater or equal to the highest experimental result. The probability p of a property x being above the highest experimentally measured property $x_{\text{exp,max}}$ can be calculated by

$$p(x \geqslant x_{\text{exp,max}})^{n_{\text{sec}}} = \frac{1}{n_{\text{spec}}}$$

$$\Longleftrightarrow p(x \geqslant x_{\text{exp,max}}) = \exp\left(\frac{1}{n_{\text{sec}}} \ln\left(\frac{1}{n_{\text{spec}}}\right)\right). \tag{8}$$

To strengthen our hypothesis we look at the limiting cases. When we test an infinite number of specimens, the possibility is close to zero for higher values of the property than found in the experiments

$$\lim_{n_{\text{spec}} \to \infty} p(x \geqslant x_{\text{exp,max}}) = 0. \tag{9}$$

Testing infinitely long specimens means we have an infinite number of sections with the property being above the highest value found in the experiments

$$\lim_{n_{\text{sec}} \to \infty} p(x \geqslant x_{\text{exp,max}}) = 1. \tag{10}$$

In other words, the more specimens we test, the better we know the boundaries of our distribution. The longer the specimens are, the less we know about the part on the right-hand side of the maximum value we measured.

Having two fixed points on the PDF, a normal distribution can be fitted by solving a nonlinear system of equations with the unknowns μ_x and σ_x

$$\begin{bmatrix} \int_{-\infty}^{x_{\text{exp,min}}} f(x;\mu_x,\sigma_x)\,\mathrm{d}x - p(x \leqslant x_{\text{exp,min}}) \\ \int_{x_{\text{exp,max}}}^{\infty} f(x;\mu_x,\sigma_x)\,\mathrm{d}x - p(x \geqslant x_{\text{exp,max}}) \end{bmatrix} = \begin{bmatrix} 0 \\ 0 \end{bmatrix}, \tag{11}$$

where $f(x;\mu_x,\sigma_x)$ is the probability density function of the experimental quantity x depending on the parameters mean μ_x and standard deviation σ_x. We use a normal distribution, since the real distribution is unknown and according to the central limit theorem, adding up independent identically distributed random effects, the overall effect tends to the normal distribution for a large number of samples. However, any other distribution with two parameters defining the shape can analogously be applied.

2.7. FEM model

FEM simulations are performed with the commercial FEM code ABAQUS/Standard 2019 considering finite deformations. Due to instabilities caused by progressive damage an implicit dynamic time integration method with a backward Euler operator is used allowing improved convergence behavior [59]. An unsymmetrical equation solver is applied since symmetry of the material Jacobian is lost when the ductile damage evolution model is applied [59]. In order to account for the differences of tensile and compressive strength of the photopolymer, an asymmetric elastoplasticity material model with continuum damage is employed capturing the progressive failure of the lattice structures. A Drucker-Prager model [69,70] is suggested by Morelle et al. [71] as good engineering practice without the need for coding a user defined subroutine for the modeling of thermosetting polymers. ABAQUS' built-in hyperbolic Drucker-Prager plasticity model is used, where the yield function Φ is given by

$$\Phi = \sqrt{\left(d'_0 - p_{\text{t0}}\tan(\beta)\right)^2 + \sigma_{\text{vM}}^2} - p\tan(\beta) - d' \leq 0, \tag{12}$$

where σ_{vM} is the von Mises equivalent stress, p is the hydrostatic pressure, β is the friction angle or the asymptotic slope in the meridional plane, p_{t0} is the initial hydrostatic tensile strength, d' is the hardening parameter and d'_0 is the initial value of the hardening parameter. The hardening parameter is obtained by

$$d'(\sigma_{\text{yt}}) = \sqrt{\left(d'_0 - p_{\text{t0}}\tan(\beta)\right)^2 + \sigma_{\text{yt}}^2} + \frac{\sigma_{\text{yt}}}{3}, \tag{13}$$

where σ_{yt} is a multilinear curve of the yield stress depending on the plastic strain from the uniaxial tensile experiments of the bulk material. For polymers, generally nonassociated flow is assumed [59]. The flow potential is given by

$$\Psi = \sqrt{\left(\epsilon\sigma_{\text{yt0}}\tan(\psi)\right)^2 + \sigma_{\text{vM}}^2} - p\tan(\psi), \tag{14}$$

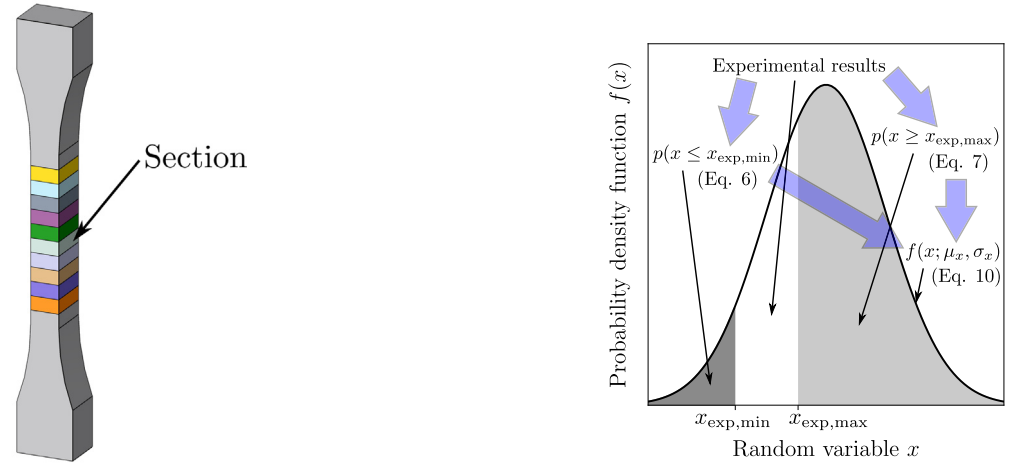

(a) Specimen sections. (b) Probability distribution model.

Fig. 5. A dog-bone specimen assumed to consist of sections with different properties (a) and procedure to determine a model for the probability distribution of local weakest link quantities (b).

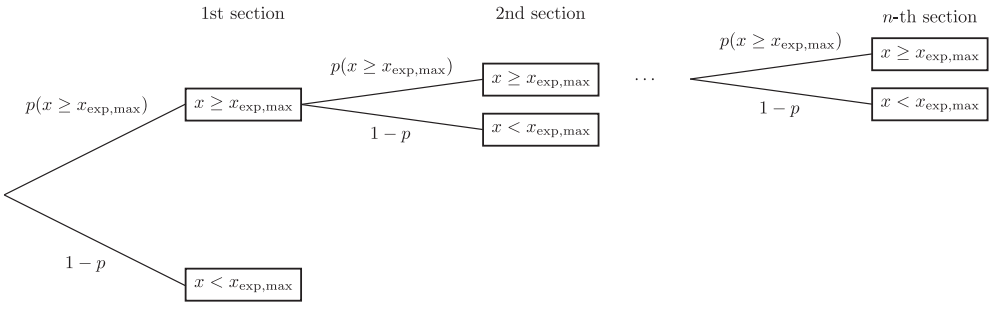

Fig. 6. Tree diagram for a specimen consisting only of sections with the property x being above the highest experimentally measured result $x_{\text{exp,max}}$ visualizing the derivation of Eq. 8.

with σ_{yt0} being the initial yield stress, ψ being the dilatation angle and ϵ being the eccentricity, a parameter determining the bending of the flow potential. ABAQUS' built-in ductile criterion is used for damage initiation as previously by Chevalier et al. [72] for a thermosetting polymer. Here, the stress-carrying capability of the element is reduced linearly when the accumulated equivalent plastic strain $\bar{\varepsilon}_p$ reaches the plastic strain at the onset of damage $\bar{\varepsilon}_{p,D}$. An energy-based damage evolution is chosen to avoid mesh dependency. Knowing the critical energy release rate G_{Ic}, the accumulated equivalent plastic strain at failure $\bar{\varepsilon}_{p,f}$ can be determined from

$$G_{Ic} = \int_{\bar{\varepsilon}_{p,D}}^{\bar{\varepsilon}_{p,f}} L\sigma_{yt}\, d\bar{\varepsilon}_p, \tag{15}$$

where L is the characteristic element length. To overcome convergence difficulties, viscous regularization is employed [59].

The material model is calibrated with the average true stress-true strain curve obtained from DIC measurements of uniaxial tensile tests on dog-bone specimens. Although polymers show a slight nonlinearity very early, we assume plastic flow to occur not before 70 % of the yield stress (defined by the horizontal tangent in the stress–strain curve in polymer standards) is reached. This reduces computational time and the deviations are small. The tension–compression asymmetry is adjusted with 70 % of the compressive yield stress analogously. Displacement controlled, single element tests on hexahedrals with uniaxial tension and compression are carried out to verify the material model. A comparison of the calibrated numerical model to the experimental tests will be later discussed in Fig. 16b.

Dog-bone specimens are simulated to validate the stochastic distribution of the material properties. All three translational degrees of freedom are fixed at one end of the bar and a tensile displacement is applied at the other end. For the discretization, ABAQUS' C3D10 tetraheadral 3D continuum elements with quadratic shape functions are utilized conforming with the simulations of the lattice structures. These allow to resolve complex three-dimensional stress fields and are able to capture the complex geometry. The elastic modulus as a global material property is homogeneous over the whole specimen but varies stochastically between the realizations. Local material properties like strength and fracture strain are assigned by random fields in the narrow parallel part of the specimen. The variation of the strength is realized by shifting the hardening law (Eq. 13) up and down. The individual sections with homogeneous material properties are chosen to be approximately 1 mm × 1 mm × 1 mm corresponding to the length of the homogeneous necking area in the DIC measurements (see Section 2.4). Basically, the sections are defined by slicing up the specimen in cubes and then assign the same material properties to all elements within one cube. Fig. 7a illustrates the individual material sections of the dog-bone specimen by different colors. Probability distributions of the material properties with the standard approach are compared with the local PDF model.

Finally, lattice structure specimens are simulated to validate the stochastic distribution of the combination of geometrical and material properties. The geometry of the lattice structures is generated with a PYTHON script, allowing for the automatic construction of parametric models. Random fields are utilized to assign individual vertical and horizontal strut diameters on the CAD geometry level. The stochastic distribution of material properties for the unit cells in the middle with no gradient in volume fraction is realized analogously to the dog-bone specimens. In order to save computational time, symmetry is used for the simulation of the lattice structures. Half of the structure is modeled and symmetry is applied in the plane normal to the loading direction. Strictly speaking, symmetry is lost due to the probabilistic variation of the quantities but in this case at least entire loaded cross sections are modeled. The deformation is displacement controlled at the end of the load introduction. A realization of a lattice structure model with individual material sections indicated by different colors is presented in Fig. 7b. Realizations with a stochastic variation of only the geometry, only the material and both combined are investigated to get insight in their individual influence.

3. Results and discussion

This section discusses the results of the study in detail and in combination. First, findings of the quality control of the post-curing by DSC and the geometrical accuracy by microscopy are presented. Then, the experimentally determined mechanical properties of the dog-bone specimens are shown and discussed within the framework of the material model and probabilistic effects. The outcome of the procedure to determine the correlation length by variography is depicted and the stochastic variations stemming from the local PDF model are demonstrated. Finally, the comparison of FEM simulations and experiments is discussed. A verification of the capabilities of the material model to capture the tension–compression asymmetry is illustrated. The probability distribution of the material properties is validated for dog-bone specimens and transferred to structures with lattice material also incorporating geometry variations.

3.1. Differential scanning calorimetry

The results of the thermal analysis by DSC are displayed in Fig. 8 with the specific heat flow depending on the temperature. The as

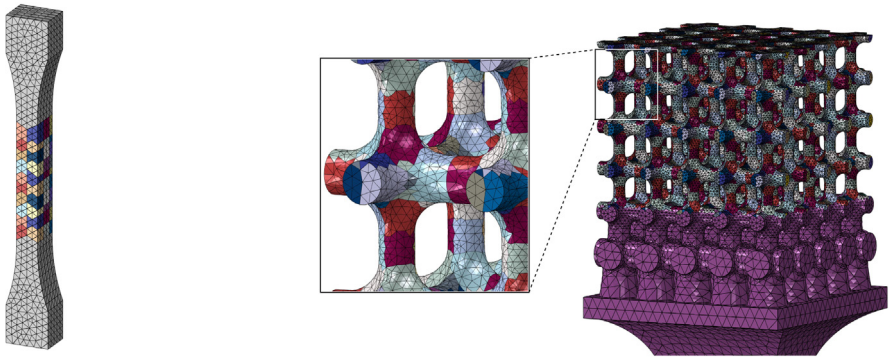

(a) Dog-bone. (b) Lattice structure.

Fig. 7. Individual material sections of the dog-bone specimens and the lattice structures in FEM models.

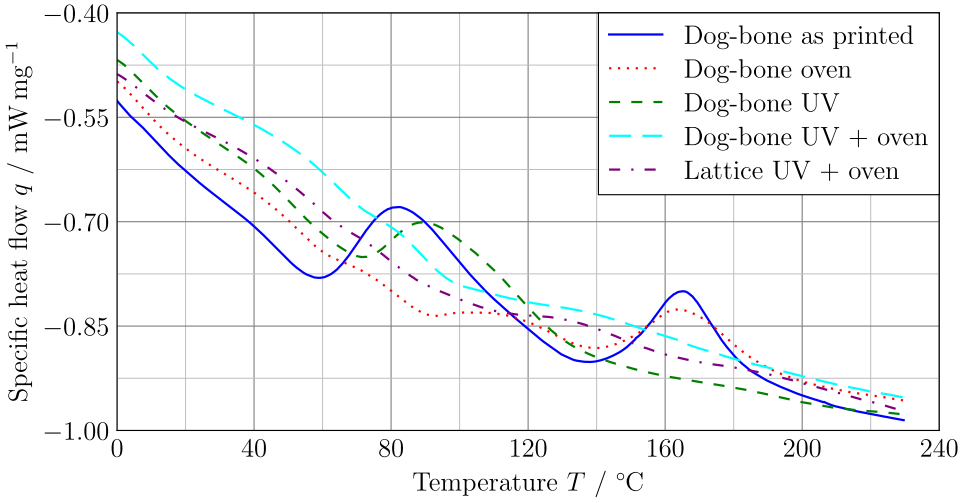

Fig. 8. First heating segment of DSC measurements showing the specific heat flow versus temperature. Exothermal flow is indicated upwards.

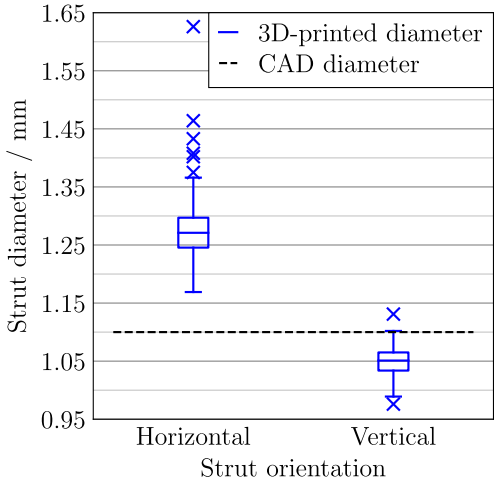

Fig. 9. Strut diameter depending on the strut orientation. The dashed black line is the desired diameter from the CAD files.

printed dog-bone specimen with no post-curing (solid blue line) shows two residual reaction enthalpy peaks: one at a temperature of approximately 80 °C and one at 165 °C. Comparing the only oven post-cured sample (dotted red line) with the only UV radiation post-cured (dashed green line), it gets evident that both curing mechanisms, temperature and UV radiation, are necessary for complete curing. The first peak vanishes almost completely by oven curing, the second peak vanishes by UV curing. For the sample from the dog-bone specimen (long-dashed cyan line) and that from within the lattice structure (dash-dotted purple line) which are both post-cured in the UV oven for 4 h, almost no residual reaction enthalpy is left and the curves match well. They have a similar curing degree and are fully cured. Higher curing temperatures are not recommended since the heat deflection temperature is reached [57].

3.2. Geometry characterization

Fig. 9 shows the results of the geometry measurements by digital microscopy. The smallest strut diameter depending on the strut orientation is shown together with the desired reference diameter from the CAD files (dashed black line). The diameter of the vertical struts is slightly smaller than the desired CAD diameter. The variation is relatively small. The diameter of the horizontal struts is significantly larger than the desired CAD diameter and shows a higher variation. There are more outliers, especially towards the larger diameters. This can be explained by the fact that the horizontal struts are printed without a support structure as an overhang. Since the 3D printer Form 2 is an inverted SLA printer, the material at the bottom of the resin bath is cured. At an overhang, also the material on top of the current layer gets residual energy from the UV laser depending on the curing depth. Thus, it is at least partially cured and leads to an increased strut diameter. As a result for modeling the geometrical variation of the strut diameters, two individual random fields are necessary, accounting for the differences in vertical and horizontal diameters. For the vertical struts, a mean of 1.049 mm and a standard deviation of 0.023 mm is used, while for the horizontal struts, a mean of 1.271 mm and a standard deviation 0.04 mm is applied.

3.3. Mechanical properties

The results of the mechanical characterization of the bulk material are summarized in Table 2 with the mean value μ and standard deviation σ. All values of the tensile and compressive tests are presented in terms of nominal quantities. The initial measuring distance L_0 for the elongation at break ε_b is 10 mm (see Sect. 2.4).

Table 2
Results of the mechanical characterization of the photopolymer resin with the number of specimens n_{spec}, mean μ and standard deviation σ.

Experiment	n_{spec}	Parameter	μ	σ
Tension	9	Modulus of elasticity E/ MPa	2200.62	39.37
		Yield stress σ_y / MPa	61.65	0.95
		Elongation at break ε_b / %	13.24	2.79
Compression	15	Yield stress σ_y / MPa	102.92	2.38
SENB	10	Critical energy release rate G_{Ic} / MPa mm	0.13	0.02

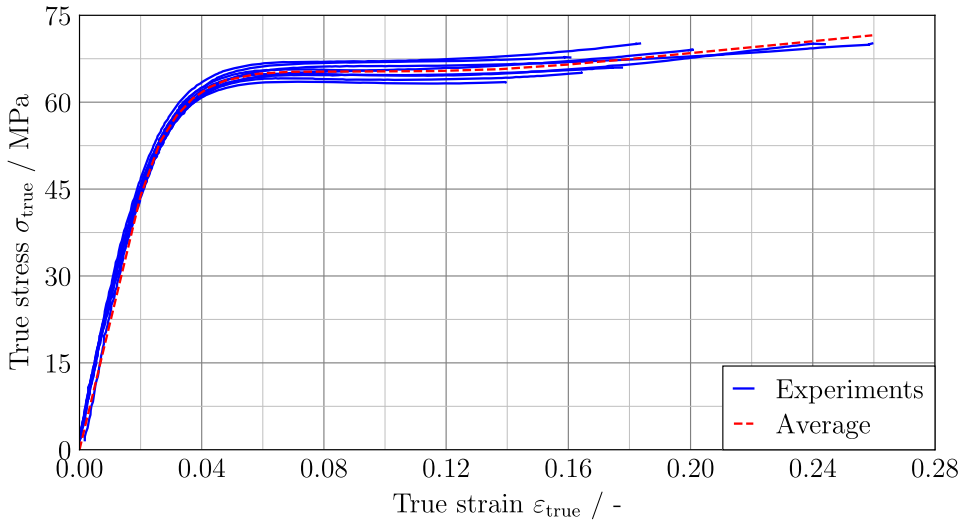

Fig. 10. True stress-true strain curves of the dog-bone specimens measured with DIC at the location of the necking.

Table 3
Kolmogorov–Smirnov tests to check if the characteristic true mechanical properties follow a normal distribution.

	E	σ_{pl}	σ_{m}	ε_{f}
p-value	0.9483	0.9997	0.9204	0.9901

The tension–compression asymmetry is very pronounced with the compressive yield stress being 67 % higher than the tensile yield stress. This underlines the necessity that a material model, such as Drucker-Prager model, considers this behavior. For the compressive specimens only the yield stress is used in this investigation, as for higher deformations significant bulging of the specimens occurs despite the use of polypropylene films to reduce friction. The deformation is not uniform anymore and a deduction of further properties would be erroneous. In the context of this study, this is not critical as the lattice structures are also primarily loaded in tension and a compressive failure is not expected. Also the Drucker-Prager material model only needs the strength differential as an input from the compressive test.

Necking occurs during the tensile testing of the dog-bone specimens. True stresses and strains necessary to calibrate the material model, cannot be derived from the nominal curves. They are obtained from DIC measurements in the necking region as described in Section 2.4. Fig. 10 shows the true stress-true strain curves of the dog-bone specimens together with the averaged curve. After an almost linear elastic regime a significant nonlinearity can be observed beyond a strain of 0.02. This is assumed to be the point where plasticity begins within the material model. From of strain of about 0.06 a rather constant stress level is reached followed by a further increase until fracture of the specimen. This can be attributed to large collective molecular movements and subsequent alignment of the molecular network until chain scisson [71]. As the level of the constant stress is characteristic for each specimen it is called plateau stress σ_{pl} in the following and taken at a strain of 0.08. When comparing the true strength σ_{m} and true fracture strain ε_{f} to their nominal counterparts, both are significantly higher. This highlights the importance of the evaluation of local stresses and strains for material modeling. The points for the multilinear curve of the yield stress for the hardening law are obtained from the averaged true stress-true strain curve (dashed red line).

In order to get more insight into the probability distributions of the characteristic true mechanical properties, Kolmogorov–Smirnov tests are carried out. The null hypothesis is that the distribution of the properties follows a normal distribution. A significance level of $\alpha = 0.05$ is chosen. Table 3 summarizes the outcome of the Kolmogorov–Smirnov tests. As the p-values are all far higher than the significance level, the null hypothesis cannot be rejected. The properties are assumed to be normally distributed.

To further explore whether there is a correlation of the characteristic true mechanical properties, they are analyzed in a scatter matrix plot in Fig. 11, where the empirical cumulative distribution functions are shown on the diagonal. The results seem to be randomly distributed over the charts with no linear or nonlinear trend visible at a first glance. Only for strength and fracture strain, a linear trend can be recognized. Hence, from the scatter plots, all variables seem to be independent except for strength and fracture strain.

To have a further measure for the independence of the true mechanical properties, the Pearson correlation coefficient is calculated. The findings are presented in Table 4 together with the corresponding p-values. The null hypothesis is that the properties are not correlated. Applying a significance level of $\alpha = 0.05$ for strength and fracture strain the null hypothesis is rejected. Thus they are assumed to depend on each other. Having a look at Fig. 10 this makes sense: when a high strain is reached, the polymer network is in a state of better alignment, thus leading to a higher strength because the polymer chains are stretched and there is less chain movement remaining. Therefore, the stress increases progressively for higher strains which results in a positive correlation. Moreover, also for plateau stress σ_{pl} and strength σ_{m} the p-value is just below the significance level, also with a slight positive correlation. For all other combinations the null hypothesis cannot be rejected. The properties are assumed to be uncorrelated. Thus, three properties are varied stochastically in the model to perform a probabilistic analysis of the material properties: (i) the elastic modulus E, (ii) the plateau stress σ_{pl} and (iii) the fracture strain ε_{f}. The latter two are applied with random fields as they are local quantities. The variation in strength is captured implicitly since the whole hardening law is scaled up and down with the plateau stress (see Section 2.7) and and depending on the fracture strain, the strength is reached earlier or later on that curve.

For the hyperbolic Drucker-Prager material model additional properties need to be identified. They are presented in Table 5. Some of them are derived from the mechanical experiments on bulk material. The Poisson's ratio is calculated from comparisons

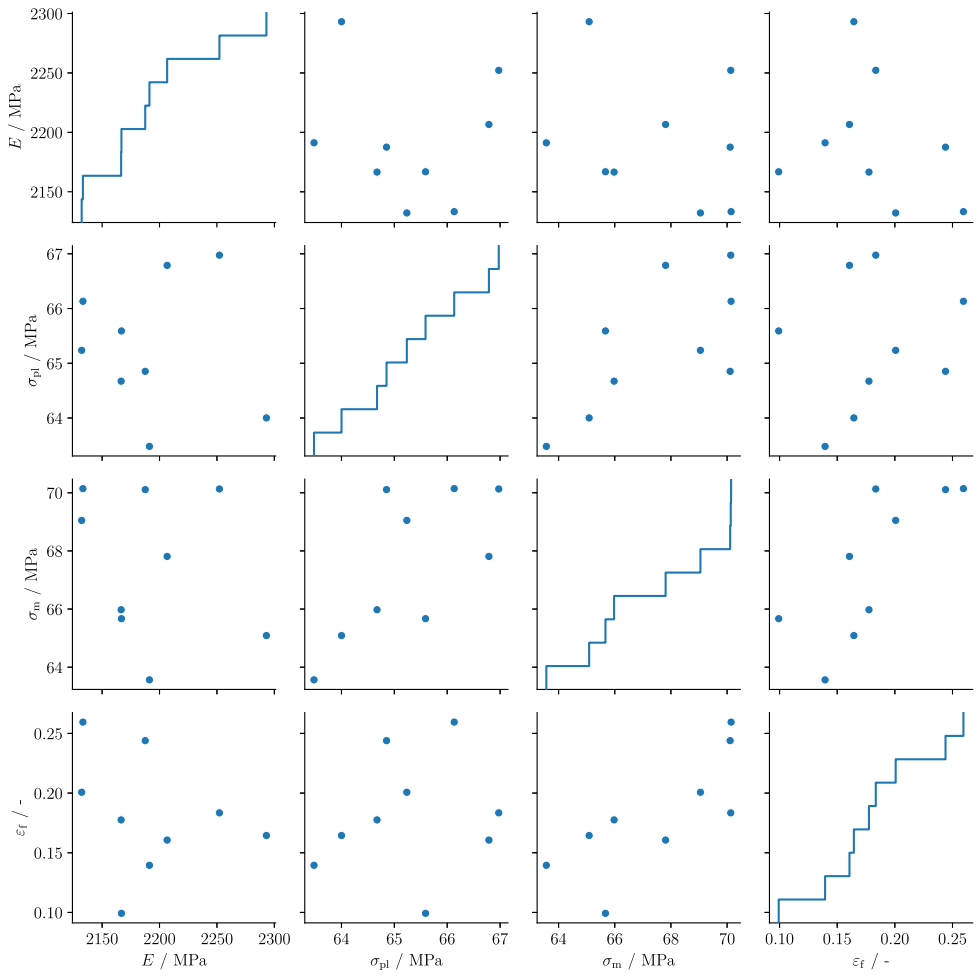

Fig. 11. Scatter matrix plot of the experimentally determined true material properties to check correlation. Empirical cumulative distribution functions are shown on the diagonal.

Table 4
Pearson correlation coefficient (and p-value) to check correlation of true material properties.

	σ_{pl}	σ_m	ε_f
E	−0.0826 (0.8326)	−0.2383 (0.5369)	−0.2726 (0.4779)
σ_{pl}		0.6908 (0.0394)	0.1801 (0.6429)
σ_m			0.7664 (0.0160)

of the longitudinal and transverse strains taken from tensile tests in the linear elastic regime. The friction angle and initial hydrostatic tensile strength are determined based on the strength differential of the yield stress. The dilatation angle is chosen to be relatively small because there is no large volume change detected from the comparison of longitudinal and transverse strain. In addition, for even smaller dilatation angles, convergence issues occur.

Table 5
Further properties for the material model.

Parameter	Value
Density ρ	1.17 g cm^{-3}
Poisson's ratio ν	0.4
Friction angle β	30 °
Initial hydrostatic tensile strength p_{t0}	44 MPa
Dilatation angle ψ	10°
Eccentricity ϵ	0.1

Finally, the density is identified by the Archimedes' principle and the eccentricity is left at the default.

From the experimental characterization of the lattice structures, homogenized mechanical properties are obtained. They are displayed in Table 6 with mean μ and standard deviation σ.

3.4. Variography

In order to determine the correlation length for the random fields of material properties and geometry deviations, variography is utilized. With regard to the material properties, it is assumed that strength and fracture strain vary on a similar length scale as they are both localized properties. With the DIC measurements, the true strain field of a specimen can be captured. It is extracted at uniformly spaced discrete points and then the point pairs are compared to generate the variogram. Fig. 12 illustrates the process for a representative dog-bone specimen and shows the semivariance depending on the separation distance of the points. A fit of the spherical model from Eq. 6 to the empirical semivariance is depicted. A correlation length of $l_c = 3.5$ mm for the material properties is extracted from the variogram. For higher separation distances, there is only a small change in the semivariance.

An exemplary realization of a random field of the plateau stress for a lattice structure model with this correlation length is displayed in Fig. 13. The standard deviation of the plateau stress depending on the spatial location within the lattice is depicted.

Table 6
Experimentally determined homogenized mechanical properties of the lattice structures.

Parameter	μ	σ
Homogenized elastic modulus E_{hom} / MPa	214.60	6.94
Homogenized strength $\sigma_{m,hom}$ / MPa	3.59	0.16
Homogenized fracture strain $\varepsilon_{f,hom}$ / %	3.18	0.75

The correlation length for the variation of the strut diameters is identified from the micrographs of the lattice structure slices. By stacking the slices on top of each other, the specimens are recreated. This results in a 3D field of the extracted strut diameters. The point pairs are then again compared to generate the variogram. The procedure together with the semivariance depending on the separation distance for the horizontal strut diameters of an exemplary lattice structure is shown in Fig. 14. Again, a fit of the spherical model from Eq. 6 to the empirical semivariance is carried out. Here, a correlation length of $l_c = 8$ mm is obtained from the variogram for the variation of the strut diameters. There is only small change in the semivariance for higher separation distances.

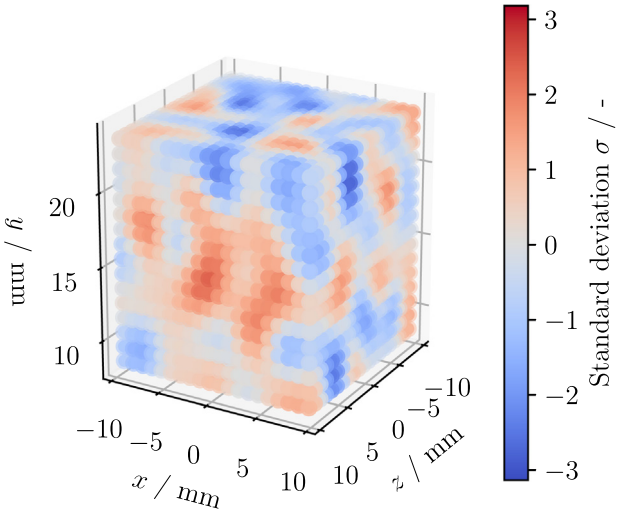

Fig. 13. Exemplary random field showing the standard deviation of the plateau stress for a lattice structure model.

3.5. Stochastic distribution of local mechanical properties

The identification of the probability distribution of material properties dominated by local effects poses a challenge. It is assumed that local defects most likely stem from the manufacturing process. Possible reasons for local defects are manifold and some are listed in the following: (i) bubbles in the resin bath, (ii) printing not perfectly in the focus of the fixed UV laser due to different positions on the build plate, (iii) partial shadowing and curing depth during post-curing, (iv) higher laser absorption of the resin bath in areas where the bottom of the bath degraded because of multiple previous exposures, (v) notches due to the removal of the support structures. Only the volume with the biggest flaw of the specimen is captured by experiments. Hence, a new method, the local PDF model (see Section 2.6) is developed and compared to the standard approach where the probability distribution is derived from the central moments of the experimental measurements directly. We assume that a dog-bone specimen consists of 10 sections with individual homogeneous material properties as the length of the homogeneous necking area in the DIC measurements is approximately 1 mm (see Section 2.4) and the parallel measuring length is 10 mm. The PDFs for both approaches are presented in Fig. 15a and b for the plateau stress σ_{pl} and the plastic failure strain $\varepsilon_{p,f}$ respectively. These are the inputs for the random fields in the FEM models. Three standard deviations are shown. For the standard approach, most of the PDF is within the range of the experimental results leaving only small tails outside of it. In case of the local PDF model, a large part of the body of the PDF is outside the range of the experimental results. For the local PDF model, the mean is shifted to higher values and the curve is flattened leading to a higher standard deviation. The shift to the right is a result of the length of the specimens since there are many sections with a higher property than the ones determined in the experiments. The flattening stems from the relatively small number of specimens tested. This leaves a lot of uncertainty of how much higher the property of the other sections can be, compared to the ones identified by the experiments.

A closer look on the PDFs for the plateau stress σ_{pl} and the plastic failure strain $\varepsilon_{p,f}$ determined with the local PDF model is dis-

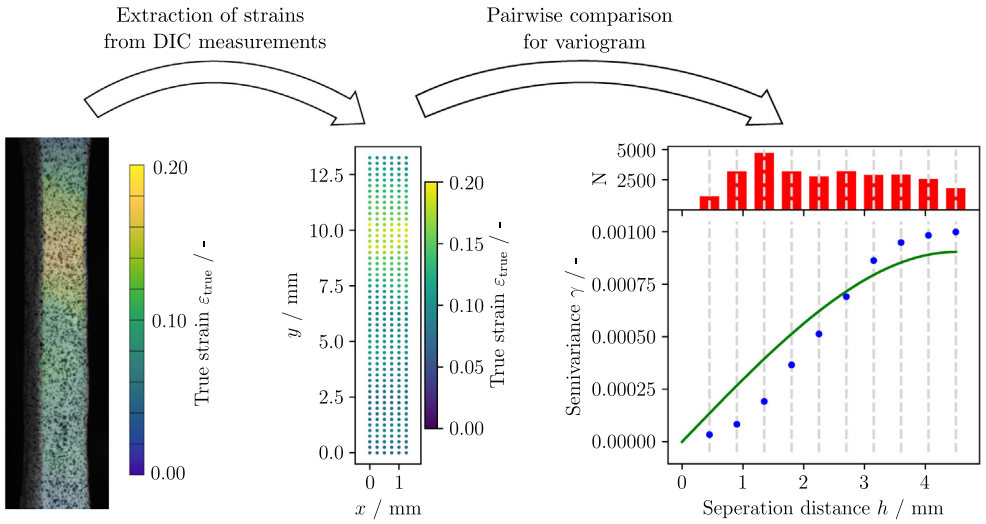

Fig. 12. Determining the correlation length of the local material properties from a variogram of the true strain of a dog-bone specimen. The point pairs are extracted from DIC measurements. The red bars show the number of point pairs at each separation distance, the blue dots depict the empirical semivariance determined with Eq. 5 and the green line is a fit of the spherical model according to Eq. 6.

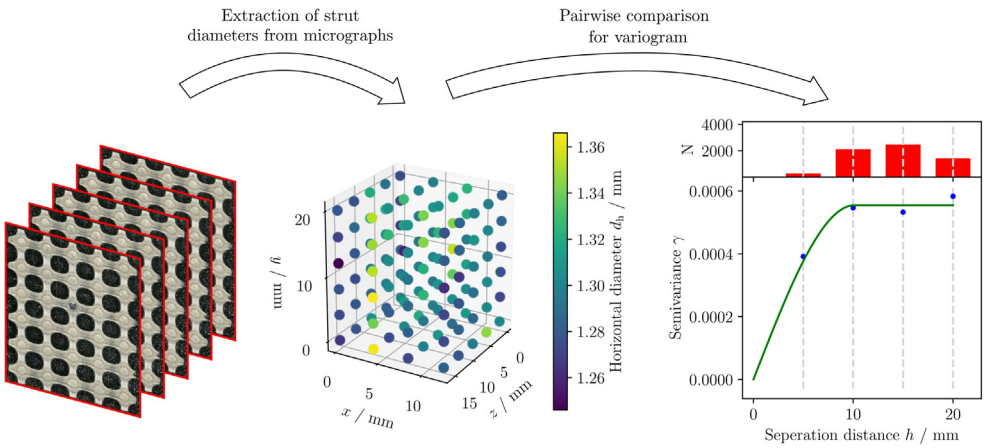

Fig. 14. Determining the correlation length of the strut diameters of the lattice structures from a variogram. The point pairs are extracted from stacked micrographs of the lattice structure specimen slices. The red bars show the number of point pairs at each separation distance, the blue dots depict the empirical semivariance determined with Eq. 5 and the green line is a fit of the spherical model according to Eq. 6.

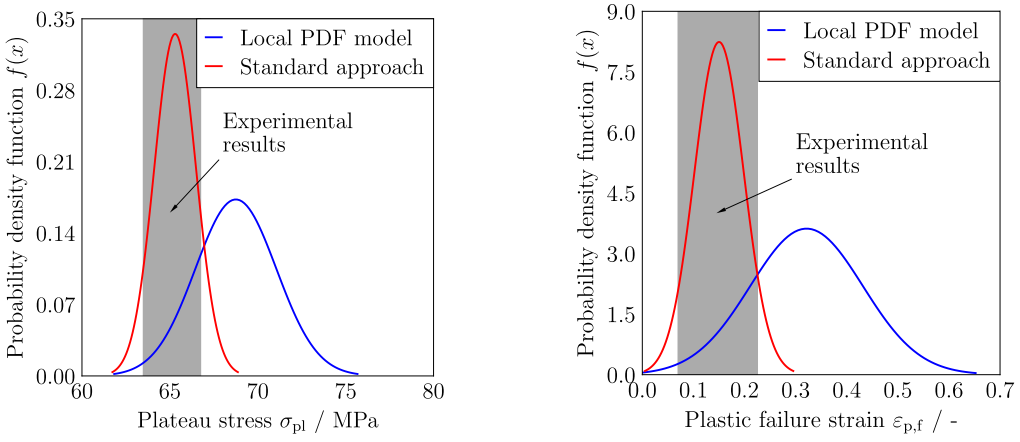

(a) Comparison σ_{pl} distributions.

(b) Comparison $\varepsilon_{p,f}$ distributions.

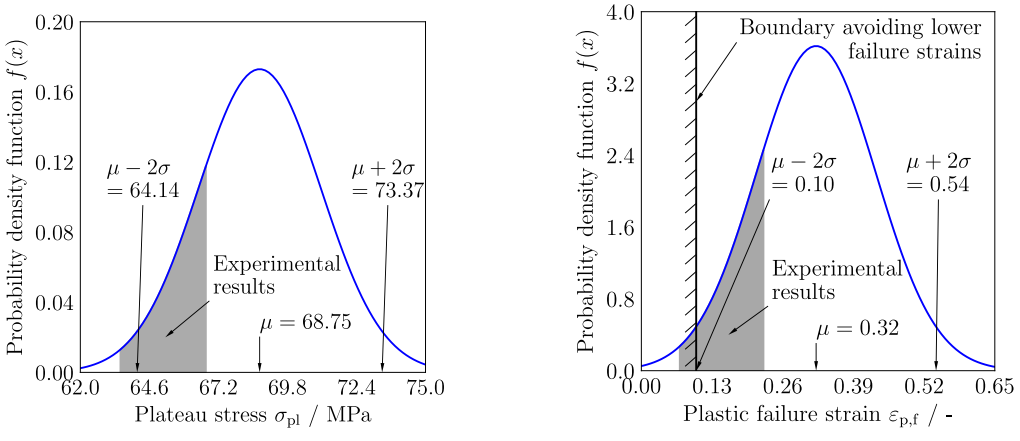

(c) Probability distribution for σ_{pl}.

(d) Probability distribution for $\varepsilon_{p,f}$.

Fig. 15. Comparison of the probability distributions for the local quantities plateau stress σ_{pl} and plastic failure strain $\varepsilon_{p,f}$ with the standard approach and the local PDF model as well as further insights in the distributions with the proposed local PDF model.

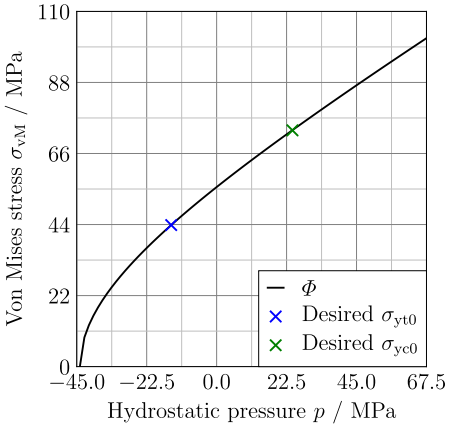

(a) Initial hyperbolic yield surface.

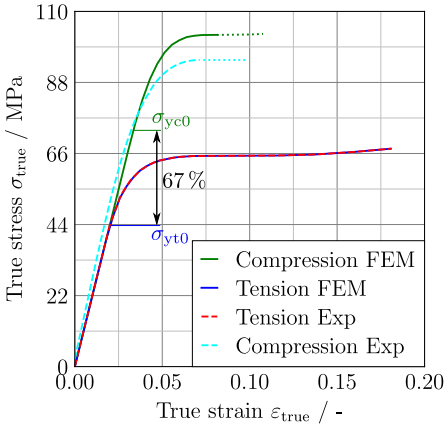

(b) Comparison of experimental average and material model in one element FEM simulations.

Fig. 16. Initial hyperbolic yield surface and comparison of the true stress-true strain curves of the experimental average and the material model in FEM. The compressive curve is not shown completely as the calibration is only for the yield point. However, higher stresses than shown are not present in the simulations later on, as the load cases are predominantly tensile.

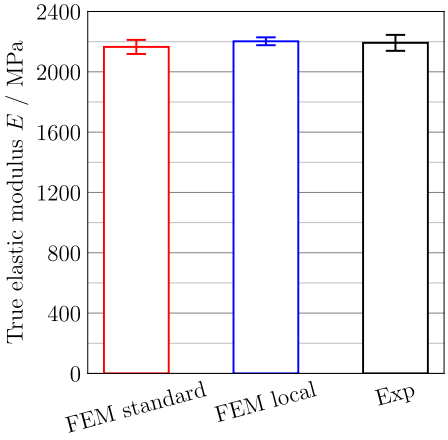

(a) True elastic modulus.

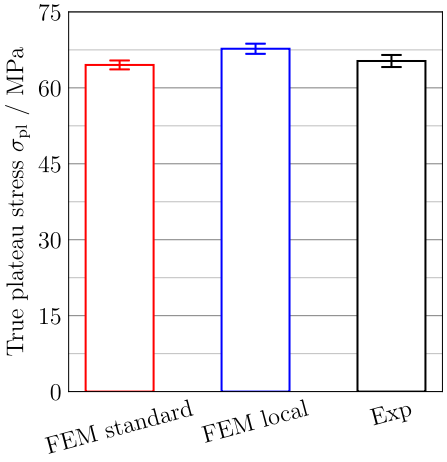

(b) True plateau stress.

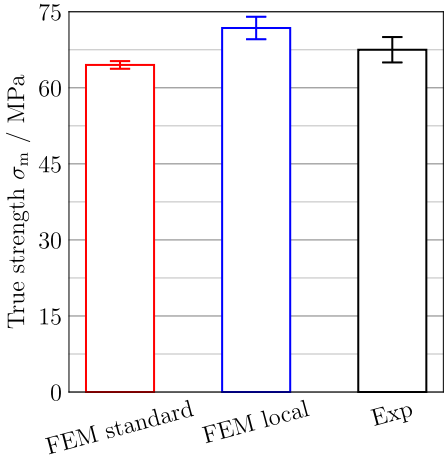

(c) True strength.

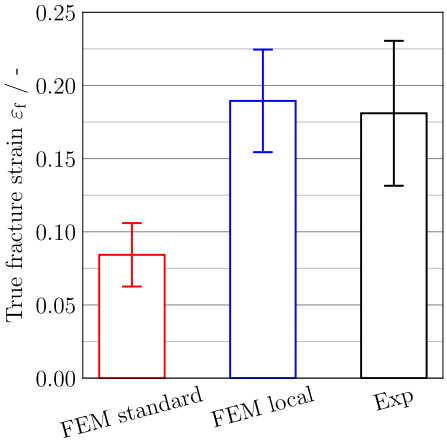

(d) True fracture strain.

Fig. 17. Comparison of the true mechanical properties for experiments and probabilistic FEM simulations of dog-bones.

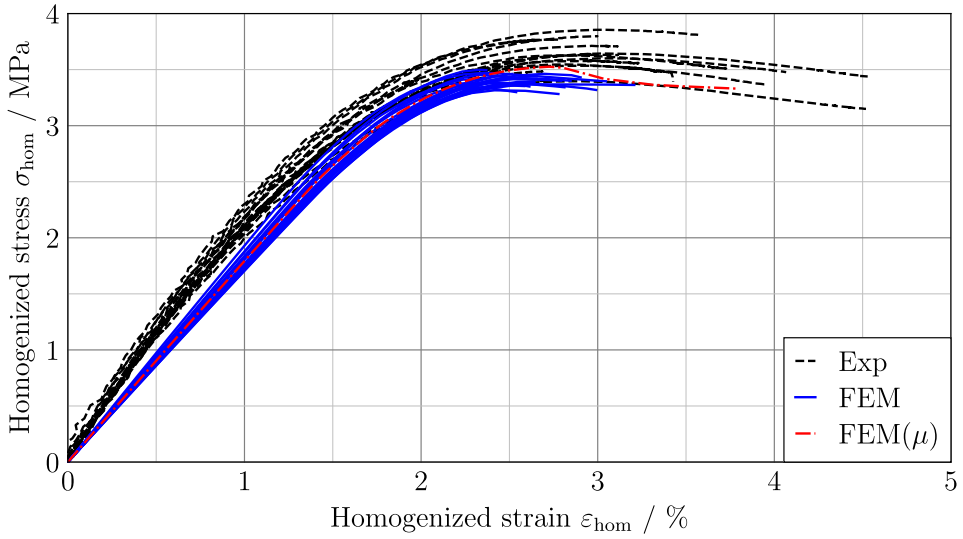

Fig. 18. Comparison of the homogenized stress–strain curves of experiments and FEM simulations of lattice structures incorporating stochastic variations of geometry and material. A FEM simulation with the mean μ for varied parameters is added.

played in Fig. 15c and d where the mean and twice the standard deviation are indicated. For the plastic failure strain, negative values can occur in the realizations which is not possible in reality. Thus, a boundary avoiding very low failure strains is applied at $\mu - 2\sigma$ leaving a truncated normal distribution.

3.6. Comparison of experiments and FEM on local level

In order to evaluate whether the proposed probabilistic approach is able to capture the stochastic variation of the experimental characterization of additively manufactured lattice structures, first the material model needs to be verified. Especially, the ability to represent the tension–compression asymmetry and therefore the material behavior under different load conditions has to be analyzed. Fig. 16a displays the initial hyperbolic yield surface obtained with the parameters identified in Section 3.3. The equivalent von Mises stress at the yield point is shown depending on the hydrostatic pressure. For an increasing hydrostatic pressure, the yield stress also increases. Both, the desired initial yield stress under tension σ_{yt0} and compression σ_{yc0} are met perfectly.

One element FEM simulations are discussed in the following to examine the differences in the mechanical response to uniaxial tensile and compressive loading. The experimental averages are compared to the one element FEM simulations in terms of the true stress-true strain curve in Fig. 16b. In the case of tensile loading, the stress–strain response coincides over the whole range: from the elastic regime, yield point and hardening to the fracture strain. Also the difference between the onset of plastic flow in tension and compression is captured well with 67 % as found in Section 3.2. The compressive curves are only considered up to the yield point since afterwards significant bulging occurs in the experiment. Thus, the stress state is not uniaxial anymore, preventing a comparison. The slight differences between the compressive curves up to that point can also stem from little bulging before the yield point. Since the true cross-section is evaluated in the middle of the compressive specimen, bulging leads to underestimation of the stress. Yet, higher compressive stresses do not occur in the structural simulations as the loading is predominantly tensile. Hence, the material model is considered to be calibrated well and able to exhibit the desired mechanical behavior.

A validation of the spatial probability distributions of the mechanical properties is carried out on the level of dog-bones. The results in terms of the true material properties are shown in Fig. 17 with the mean and standard deviation. The experimental results are compared with 10 realizations of FEM models with probability distributions for the local properties derived from the standard approach (FEM standard) and the local PDF model (FEM local). The true properties in the FEM simulations are captured in a similar way as in the experiments by tracking the distance change between two points in longitudinal and transversal direction in the region of the necking. With regard to the true elastic modulus, the results are in accordance with each other. The elastic modulus is a global property, hence it is applied exactly the same in both FEM models. Therefore, a difference is not expected. Concerning the true plateau stress and especially the true strength, the FEM standard simulations slightly underestimate and the FEM local simulations slightly overestimate the properties compared to the experiments. In the case of the true strength, the standard deviation of the FEM local simulations is in a similar range as in the experiments, while in the FEM standard simulations it is smaller. The difference of the FEM local simulations can be explained when having a look at the PDF in Section 3.5. The number of specimens tested in the experiments together with their length results in a large standard deviation and a higher mean. Since the realizations of the FEM models have a rather small volume where the material properties are varied, the larger mean dominates. Despite the higher standard deviation, not that many low values occur. Testing more specimens in the experiments would reduce the uncertainty in the local PDF approach, thus leading to a smaller part of the body of the PDF being on the right-hand side of the experimentally determined property. Having a look at the true fracture strain, very similar results are obtained with the FEM local simulations and experiments. In contrast, the FEM standard simulations show significantly smaller fracture strains and also a smaller standard deviation. Here, the inability of the standard approach to capture the probability distribution of the local property gets clearly evident. The probability distribution is obtained based on the property of the worst section of the specimens in the experiments and then distributed over the whole model in the simulation. This results in realizations with artificially low properties. In summary, the FEM simulations with local PDF

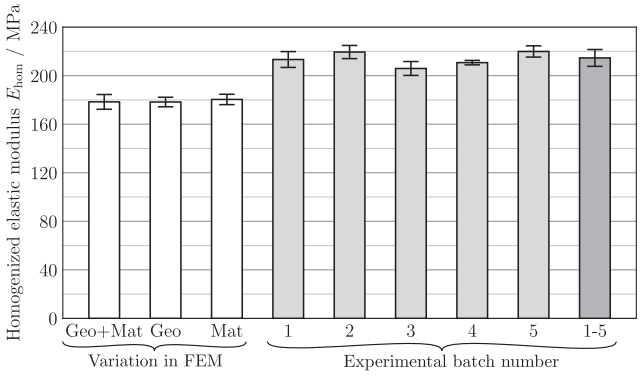

(a) Elastic modulus.

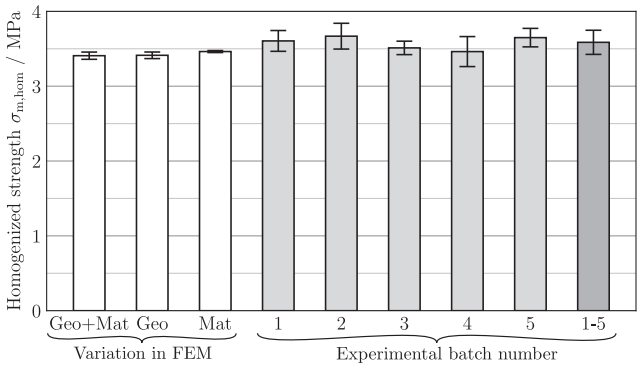

(b) Strength.

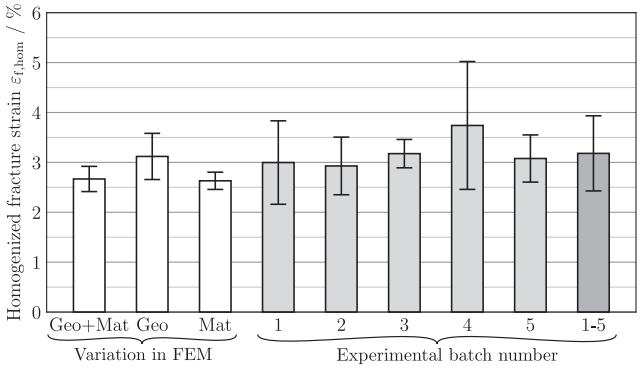

(c) Fracture strain.

Fig. 19. Comparison of the homogenized mechanical properties for experiments and simulations of lattice structures. Experiments are also shown batch-wise. For FEM simulations the variation of geometry and material are shown separately, as well as in combination.

model show only small deviations from the experiments in strength and capture the fracture strain very well. Hence, the newly proposed model outperforms the standard approach and is used in the following for the lattice structures. With regard to the progression of the plastic deformation, the necking and the fracture, the region with the lowest plateau stress in the random field of a model is decisive. Here, the localization takes place. The fracture strain of the specimens then depends on the plastic failure strain of that section.

3.7. Comparison of experiments and FEM on global level

Having seen the ability of the newly proposed local PDF model to capture the stochastic distribution of the mechanical properties, a transfer to more complex structures is carried out. FEM simulations of lattice structures with varying material properties are conducted. Also the variation in geometrical accuracy is investigated because it plays a role for more complex structures. Fig. 18 shows a comparison of the homogenized stress–strain curves of the lattice structures for experiments as well as for 20 realizations of FEM models with a variation of material properties and geometry. Additionally, the homogenized stress–strain response of an FEM model is displayed, where all varying properties are set to the mean μ. When comparing the FEM simulation with the experiments, the general trend is represented well. Also a significant amount of the variation can be described. However, the homogenized stiffness seems to be slightly underestimated and the homogenized strength and fracture strain are at the lower half of the distributions. Since the homogenized elastic modulus is too low, the material properties can be slightly different in the lattice structure experiments compared to the bulk material. A size effect could be responsible, as the individual struts have a smaller volume than the bulk dog-bones. It can as well be a result of the cross-linking density of the photopolymer since it develops by a radical reaction mechanism. Thus, the resulting termination speed of the reaction by radical recombination depends on the process parameters. Higher concentrations of radicals due to higher UV intensity can lead to earlier termination [73]. Also depending on the network that has already developed during curing and the ambient temperature, the chain mobility and thus further progress of the reaction is limited [74]. Despite being fully cured as shown by DSC measurements in Section 3.1 this can lead to different networks. For instance, within the post-curing process, the unequal specimen volumes can lead to different heating rates. Different UV intensities can occur due to partial shadowing or depending on the curing depth for structures with different volumes. Interestingly, the FEM model with mean properties shows the highest strength and elongation at break. All other FEM simulations are below the mean model. Similar to the dog-bones but with the opposite effect, this can be explained by the local PDF model for the material properties. The volume of the lattice structure specimens, where the material properties are varied, is large compared to the volume of the dog-bones. Hence, the large standard deviation of the local PDF model due to the limited number of experiments for the calibration dominates. This leads to low values of the property occurring in the larger volume of almost every lattice structure realization. Since the biggest flaw determines the overall behavior of the specimen for the local mechanical properties, this leads to an inferior performance of most of the realizations compared to the mean FEM model.

To get deeper insights in the behavior of the lattice structures, the homogenized mechanical properties of the lattice structures are presented in Fig. 19 with the mean an the standard deviation. The experimental results are separated batch-wise according to each printing process where 5 lattice structure specimens are manufactured together. However, a certain amount of specimens was not generated correctly so the batches comprise different numbers of analyzed specimens: 3 specimens for batch 1 and 3; 4 specimens for batch 4 and 5; and 5 specimens for batch 2, respectively. In addition, an advantage of the FEM modeling is exploited: the automatic model generation not only allows to analyze the probabilistic effects of geometry deviations and material properties (Geo + Mat) together, but can also separate the influence of geometry deviations (Geo) and material properties (Mat) from each other. When the probabilistic variation of the geometry deviations is explored, the material is kept constant at the mean and vice versa. For both cases, 10 realizations of the model are analyzed. Regarding the experiments, significant differences between the individual batches can be found. For example, the homogenized elastic modulus of batch 3 is significantly lower and the standard

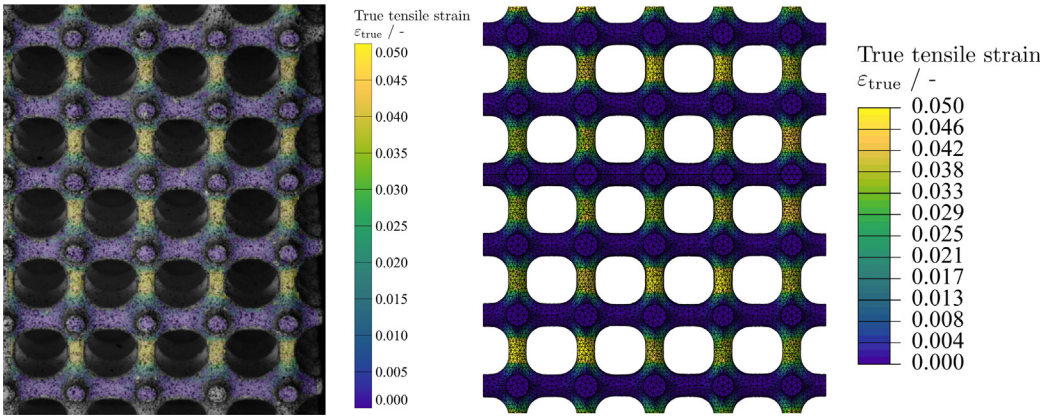

(a) Experiments. (b) Simulations.

Fig. 20. Comparison of the DIC and FEM contour plots of the true local strain in loading direction for a lattice specimen at a homogenized strain of $\varepsilon_{hom} = 0.023$ appearing approximately at the strength σ_m of the specimen.

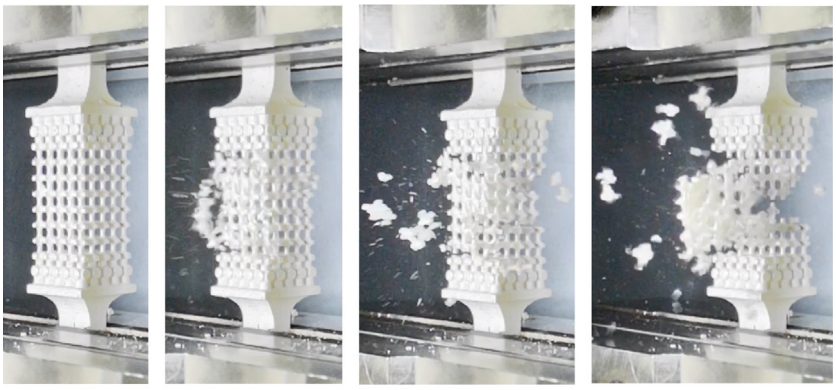

(a) Experiments.

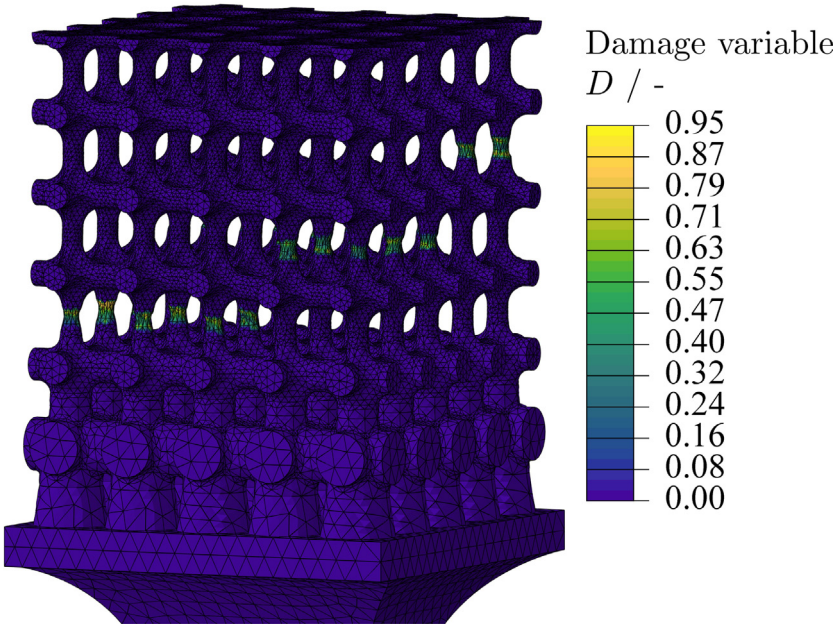

(b) Simulations.

Fig. 21. Stochastic damage of the lattice structures visible in slow motion video frames of the experiments and in a contour plot of the damage variable in FEM simulations.

deviation of batch 4 is very small compared to the others. In contrast, the standard deviation of the homogenized fracture strain of batch 4 is extremely high, as it includes the 3 specimens with the highest strains in the experiments. Differences between the batches indicate that there are additional influences during the specimen preparation that were not considered beforehand. Further effects could be the age of the resin and the resin bath, time between printing and post-curing, time between post-curing and testing as well as moisture absorption. Also the position of the specimen in the printer can influence the mechanical properties because the distance of the fixed UV source is different for the center and the border of the build plate yielding issues with the laser focus.

Concerning the FEM simulations, it can be seen that for a global property like the homogenized elastic modulus the effects of the variation of geometry deviations and material properties are similar and that they superimpose when combined leading to a higher standard deviation. The standard deviation is similar compared to the experimental one, although it is on a lower level. For local properties like homogenized strength and fracture strain, one of the influences dominates. In case of the homogenized strength, the geometry deviations dominate as the biggest flaw. The Geo realizations have a similar mean and standard deviation as the combined models. For the homogenized fracture strain, the variation in material properties dominates leading to earlier failure. This yields a similar mean and standard deviation of the Mat realizations and the combined models.

Having a closer look at the homogenized fracture strain in the experiments, significantly lower values are noticeable for the lattice structures compared to the elongation at break of the dog-bone specimens in Section 3.3. DIC measurements and FEM simulations help to clarify this. Contour plots of the true local strain in loading direction of DIC measurements and FEM simulations are illustrated in Fig. 20 at the instance, when the homogenized strength is reached. In case of FEM, the model is mirrored at the horizontal symmetry plane to have a more similar optical impression. DIC and FEM are in good agreement. Local strain concentrations can be seen at the smallest diameter of the struts in loading direction. Therefore, the discrepancy between the fracture strains of dog-bone specimens and lattice structures can be explained by the inhomogeneities in the strain field of the lattice structures. Especially for the FEM simulation slight differences between the strains in the individual struts are visible owing to the geometry and material variations with random fields. FEM simulations can give further insights as also the inner cells can be inspected.

FEM simulations also allow to study the failure mechanisms after the plastic regime. Fig. 21 shows the damage progression in frames of a slow motion video of the experiment and a contour plot of the damage variable in an exemplary FEM simulation. Due to the probabilistic variation of geometry and material properties, a stochastic failure pattern develops. The fracture jumps between different planes of the lattice. Hence, experiments and FEM simulations also match well in the last part of the material test. The stochastic nature of the failure pattern further indicates, that the gradient at the load introduction serves its purpose and prevents an early failure due to a stiffness jump as in other studies [75,76,35]. Thus, it delivers reliable results in tensile tests of the homogenized mechanical properties of lattice structures.

4. Conclusion

In this study, the probabilistic effects of the variation of geometry deviations and material properties are analyzed for SLA manufactured lattice structures. Geometry variations of the lattice struts are extracted from micrographs. Basic mechanical tests (tension, compression and SENB) on bulk material combined with DIC measurements are performed to determine the variation of the material properties. The correlation length of probabilistic effects is determined with variography. In order to identify the probability distribution of local material properties like strength and fracture strain, a new model is developed. Finally, FEM simulations incorporating the previously determined probabilistic influences are compared to experiments with lattice structures in terms of homogenized mechanical properties and failure mechanisms.

The probability distribution of the mechanical properties of lattice structures can be estimated with FEM simulations incorporating stochastic variations of geometry deviations and material properties. Good agreement is found over the whole stress–strain response and the failure progression.

With regard to the stochastic distribution of material properties, global ones like the elastic modulus and properties like strength and fracture strain, that are governed by local effects such as necking, need to be distinguished. While the probability distribution of the elastic modulus can be identified from the central moments of the experimental results of the bulk material characterization specimens, this is not possible for the local properties. Here, the experiments only show the weakest part of the specimens. Distributing these properties over the whole specimen leads to an underestimation in the FEM models. Hence a new approach, the local PDF model, is developed. It proves to be able to determine the probability distribution of local properties well and outperforms the standard approach with the central moments.

Moreover, variography is found to be a valuable tool to determine the correlation length of varying properties. The correlation length allows to determine random fields of the properties for the models. Especially in combination with DIC measurements, the strain fields can be easily evaluated. DIC measurements also enable the resolution of local phenomena like necking and therefore permit to determine true material properties in tensile tests. A further finding of the material characterization is the strong tension–compression asymmetry of the photopolymer. This is captured well by a hyperbolic Drucker-Prager material model in the FEM simulations.

This work also highlights the necessity to incorporate probabilistic effects into the design procedure in order to manufacture robust structures especially in lightweight design, where huge safety factors are not tolerable. This is crucial for manufacturing processes like 3D printing, which are more prone to exhibit imperfections. FEM simulations are advantageous as they allow to distinguish the influence of the variation of individual effects. The approach presented can be applied to other unit cell types, additive manufacturing processes and/or materials. Therefore, guidelines for a design engineer to evaluate the potential of lattice structures for lightweight purposes from a robust design perspective with the proposed modelling approach are summarized below:

- Determine the probability distributions and correlation lengths of the relevant input parameters (material properties, geometry, loads) with simple experiments
- Generate a model incorporating the varying parameters by random fields
- Validate the model with regard to the simple experiments on the input parameters
- Determine the probability distribution of the performance of the structural components subject to all varying input parameters
- Perform a (weak) validation of the performance of the structural components by a small number of experiments
- Analyze the influence of individual input parameters on the performance of the structure with the model

- Evaluate whether improvements regarding the robustness of the most influential input parameters are possible to enhance the robustness of the performance of the structure
- Compare the probability to be below a certain performance level and the weight savings for lattice structures to conventionally manufactured lightweight components

This procedure can be applied in a multi-scale homogenization framework to determine the effective properties of lattice structures on a micro-scale, which are required for accurate simulations with nonlinear material models on larger scales.

Data availability

The raw/processed data required to reproduce these findings cannot be shared at this time as the data also forms part of an ongoing study.

CRediT authorship contribution statement

Sven Drücker: Conceptualization, Methodology, Software, Validation, Formal analysis, Investigation, Data Curation, Writing - Original Draft, Visualization, Project administration. **Julian Kajo Lüdeker:** Conceptualization, Software, Formal analysis, Writing - Review & Editing, Project administration. **Marvin Blecken:** Validation, Formal analysis, Investigation, Writing - Review & Editing. **Arne Kurt:** Software, Investigation, Writing - Review & Editing. **Kirill Betz:** Validation, Investigation, Writing - Review & Editing. **Benedikt Kriegesmann:** Conceptualization, Software, Resources, Writing - Review and Editing, Supervision, Project administration, Funding acquisition. **Bodo Fiedler:** Conceptualization, Resources, Writing - Review & Editing, Supervision, Project administration, Funding acquisition.

Declaration of competing interest

The authors declare that they have no known competing financial interests or personal relationships that could have appeared to influence the work reported in this paper.

Acknowledgement

The authors thank Karl Schulte for the constructive feedback and fruitful discussions. Financial support from the Zentrum für Hochleistungsmaterialien (ZHM) in the project "Probabilistische Analyse & Entwurfsoptimierung additiv gefertigter Gitterstrukturen" is gratefully acknowledged. We acknowledge support for the Open Access fees by Hamburg University of Technology (TUHH) in the funding program Open Access Publishing.

References

[1] L.J. Gibson, M.F. Ashby, Cellular Solids: Structure and Properties, in: Cambridge Solid State Science Series, 2nd ed., Cambridge University Press, 1997. doi:10.1017/CBO9781139878326.
[2] M.F. Ashby, A.G. Evans, N.A. Fleck, L.J. Gibson, J.W. Hutchinson, H.N.G. Wadley, Metal Foams: A Design Guide, Butterworth-Heinemann, 2000.
[3] N.A. Fleck, V.S. Deshpande, M.F. Ashby, Micro-architectured materials: past, present and future, Proc. Roy. Soc. A: Math., Phys. Eng. Sci. 466 (2010) 2495–2516, https://doi.org/10.1098/rspa.2010.0215.
[4] M. Osanov, J.K. Guest, Topology optimization for architected materials design, Annu. Rev. Mater. Res. 46 (1) (2016) 211–233, https://doi.org/10.1146/annurev-matsci-070115-031826.
[5] J. Liu, A.T. Gaynor, S. Chen, Z. Kang, K. Suresh, A. Takezawa, L. Li, J. Kato, J. Tang, C.C.L. Wang, L. Cheng, X. Liang, A.C. To, Current and future trends in topology optimization for additive manufacturing, Structural and Multidisciplinary Optimization 57 (6) (2018) 2457–2483, https://doi.org/10.1007/s00158-018-1994-3.
[6] O. Sigmund, Materials with prescribed constitutive parameters: an inverse homogenization problem, Int. J. Solids Struct. 31 (17) (1994) 2313–2329, https://doi.org/10.1016/0020-7683(94)90154-6.
[7] C. Hutter, D. Büchi, V. Zuber, P.R. von Rohr, Heat transfer in metal foams and designed porous media, Chem. Eng. Sci. 66 (17) (2011) 3806–3814, https://doi.org/10.1016/j.ces.2011.05.005.
[8] T. Wu, K. Liu, A. Tovar, Multiphase topology optimization of lattice injection molds, Computers & Structures 192 (2017) 71–82, https://doi.org/10.1016/j.compstruc.2017.07.007.
[9] H. Zhou, X. Zhang, H. Zeng, H. Yang, H. Lei, X. Li, Y. Wang, Lightweight structure of a phase-change thermal controller based on lattice cells manufactured by SLM, Chin. J. Aeronaut. 32 (7) (2019) 1727–1732, https://doi.org/10.1016/j.cja.2018.08.017.
[10] S. Arabnejad Khanoki, D. Pasini, Fatigue design of a mechanically biocompatible lattice for a proof-of-concept femoral stem, J. Mech. Behav. Biomed. Mater. 22 (2013) 65–83, https://doi.org/10.1016/j.jmbbm.2013.03.002.
[11] W.-M. Chen, Y.M. Xie, G. Imbalzano, J. Shen, S. Xu, S.-J. Lee, P.V.S. Lee, Lattice Ti structures with low rigidity but compatible mechanical strength: Design of implant materials for trabecular bone, International Journal of Precision Engineering and Manufacturing 17 (6) (2016) 793–799, https://doi.org/10.1007/s12541-016-0097-6.
[12] M. Klumpp, A. Inayat, J. Schwerdtfeger, C. Körner, R.F. Singer, H. Freund, W. Schwieger, Periodic open cellular structures with ideal cubic cell geometry: Effect of porosity and cell orientation on pressure drop behavior, Chem. Eng. J. 242 (2014) 364–378, https://doi.org/10.1016/j.cej.2013.12.060.
[13] A. Olenberg, W. Reschetnik, G. Kullmer, E.Y. Kenig, Optimization of structured packings using twisted tape inserts, Chem. Eng. Res. Des. 132 (2018) 1–8, https://doi.org/10.1016/j.cherd.2017.12.036.
[14] G. Do, M. Geißelbrecht, W. Schwieger, H. Freund, Additive manufacturing of interpenetrating periodic open cellular structures (interpocs) with in operando adjustable flow characteristics, Chemical Engineering and Processing - Process Intensification 148 (2020) 107786, https://doi.org/10.1016/j.cep.2019.107786.
[15] M. Bici, S. Brischetto, F. Campana, C.G. Ferro, C. Seclì, S. Varetti, P. Maggiore, A. Mazza, Development of a multifunctional panel for aerospace use through SLM additive manufacturing, Procedia CIRP 67 (2018) 215–220, https://doi.org/10.1016/j.procir.2017.12.202.
[16] M. Ashby, The properties of foams and lattices, Philosophical Transactions of the Royal Society A: Mathematical, Physical and Engineering Sciences 364 (2006) 15–30, https://doi.org/10.1098/rsta.2005.1678.
[17] O. Sigmund, On the optimality of bone microstructure, in: P. Pedersen, M.P. Bendsœ(Eds.), IUTAM Symposium on Synthesis in Bio Solid Mechanics, Springer, Kluwer Academic Publishers, 1999, pp. 221–234. doi:10.1007/0-306-46939-1_20.
[18] Z. Xiao, Y. Yang, R. Xiao, Y. Bai, C. Song, D. Wang, Evaluation of topology-optimized lattice structures manufactured via selective laser melting, Materials & Design 143 (2018) 27–37, https://doi.org/10.1016/j.matdes.2018.01.023.
[19] B.N. Vu, F. Wein, M. Stingl, Two-scale optimization and generation of anisotropic cellular designs in the context of additive manufacturing, Comput. Aided Des. 140 (2021) 103073, https://doi.org/10.1016/j.cad.2021.103073.
[20] T. Maconachie, M. Leary, B. Lozanovski, X. Zhang, M. Qian, O. Faruque, M. Brandt, SLM lattice structures: Properties, performance, applications and challenges, Materials & Design 183 (2019) 108137, https://doi.org/10.1016/j.matdes.2019.108137.
[21] B. Gorny, T. Niendorf, J. Lackmann, M. Thoene, T. Troester, H. Maier, In situ characterization of the deformation and failure behavior of non-stochastic porous structures processed by selective laser melting, Materials Science and Engineering: A 528 (27) (2011) 7962–7967, https://doi.org/10.1016/j.msea.2011.07.026.
[22] M. Mazur, M. Leary, S. Sun, M. Vcelka, D. Shidid, M. Brandt, Deformation and failure behaviour of Ti-6Al-4V lattice structures manufactured by selective laser melting (SLM), The International Journal of Advanced Manufacturing Technology 84 (2016) 1391–1411, https://doi.org/10.1007/s00170-015-7655-4.
[23] M. Leary, M. Mazur, J. Elambasseril, M. McMillan, T. Chirent, Y. Sun, M. Qian, M. Easton, M. Brandt, Selective laser melting (SLM) of AlSi12Mg lattice structures, Materials & Design 98 (2016) 344–357, https://doi.org/10.1016/j.matdes.2016.02.127.
[24] M. Leary, M. Mazur, H. Williams, E. Yang, A. Alghamdi, B. Lozanovski, X. Zhang, D. Shidid, L. Farahbod-Sternahl, G. Witt, I. Kelbassa, P. Choong, M. Qian, M. Brandt, Inconel 625 lattice structures manufactured by selective laser melting (SLM): Mechanical properties, deformation and failure modes, Materials & Design 157 (2018) 179–199, https://doi.org/10.1016/j.matdes.2018.06.010.
[25] P. Li, Z. Wang, N. Petrinic, C. Siviour, Deformation behaviour of stainless steel microlattice structures by selective laser melting, Materials Science and Engineering: A 614 (2014) 116–121, https://doi.org/10.1016/j.msea.2014.07.015.
[26] L. Boniotti, S. Beretta, L. Patriarca, L. Rigoni, S. Foletti, Experimental and numerical investigation on compressive fatigue strength of lattice structures of AlSi7Mg manufactured by SLM, Int. J. Fatigue 128 (2019) 105181, https://doi.org/10.1016/j.ijfatigue.2019.06.041.
[27] C. Ling, A. Cernicchi, M.D. Gilchrist, P. Cardiff, Mechanical behaviour of additively-manufactured polymeric octet-truss lattice structures under quasi-static and dynamic compressive loading, Materials & Design 162 (2019) 106–118, https://doi.org/10.1016/j.matdes.2018.11.035.

[28] B. Lozanovski, M. Leary, P. Tran, D. Shidid, M. Qian, P. Choong, M. Brandt, Computational modelling of strut defects in SLM manufactured lattice structures, Materials & Design 171 (2019) 107671, https://doi.org/10.1016/j.matdes.2019.107671.
[29] P. Li, Constitutive and failure behaviour in selective laser melted stainless steel for microlattice structures, Materials Science and Engineering: A 622 (2015) 114–120, https://doi.org/10.1016/j.msea.2014.11.028.
[30] Y. Amani, S. Dancette, P. Delroisse, A. Simar, E. Maire, Compression behavior of lattice structures produced by selective laser melting: X-ray tomography based experimental and finite element approaches, Acta Mater. 159 (2018) 395–407, https://doi.org/10.1016/j.actamat.2018.08.030.
[31] V.S. Deshpande, N.A. Fleck, M.F. Ashby, Effective properties of the octet-truss lattice material, J. Mech. Phys. Solids 49 (8) (2001) 1747–1769, https://doi.org/10.1016/S0022-5096(01)00010-2.
[32] Z. Wang, P. Li, Characterisation and constitutive model of tensile properties of selective laser melted Ti-6Al-4V struts for microlattice structures, Materials Science and Engineering: A 725 (2018) 350–358, https://doi.org/10.1016/j.msea.2018.04.006.
[33] P. Baranowski, P. Płatek, A. Antolak-Dudka, M. Sarzyński, M. Kucewicz, T. Durejko, J. Małachowski, J. Janiszewski, T. Czujko, Deformation of honeycomb cellular structures manufactured with Laser Engineered Net Shaping (LENS) technology under quasi-static loading: Experimental testing and simulation, Additive Manufacturing 25 (2019) 307–316, https://doi.org/10.1016/j.addma.2018.11.018.
[34] J.P. Oliveira, A.D. LaLonde, J. Ma, Processing parameters in laser powder bed fusion metal additive manufacturing, Materials & Design 193 (2020) 108762, https://doi.org/10.1016/j.matdes.2020.108762.
[35] S. Drücker, M. Schulze, H. Ipsen, L. Bandegani, H. Hoch, M. Kluge, B. Fiedler, Experimental and numerical mechanical characterization of additively manufactured Ti6Al4V lattice structures considering progressive damage, Int. J. Mech. Sci. 189 (2021) 105986, https://doi.org/10.1016/j.ijmecsci.2020.105986.
[36] A. Haldar, S. Mahadevan, Probability, Reliability and Statistical Methods in Engineering Design, John Wiley & Sons, 1999.
[37] G. Stefanou, The stochastic finite element method: Past, present and future, Comput. Methods Appl. Mech. Eng. 198 (9–12) (2009) 1031–1051, https://doi.org/10.1016/j.cma.2008.11.007.
[38] J.D. Arregui-Mena, L. Margetts, P.M. Mummery, Practical application of the stochastic finite element method, Archives of Computational Methods in Engineering 23 (1) (2014) 171–190, https://doi.org/10.1007/s11831-014-9139-3.
[39] B. Kriegesmann, R. Rolfes, C. Hühne, J. Teßmer, J. Arbocz, Probabilistic design of axially compressed composite cylinders with geometric and loading imperfections, Int. J. Struct. Stab. Dyn. 10 (4) (2010) 623–644, https://doi.org/10.1142/S0219455410003658.
[40] J.K. Lüdeker, O. Sigmund, B. Kriegesmann, Inverse homogenization using isogeometric shape optimization, Comput. Methods Appl. Mech. Eng. 368 (2020) 113170, https://doi.org/10.1016/j.cma.2020.113170.
[41] B. Kriegesmann, R. Rolfes, C. Hühne, A. Kling, Fast probabilistic design procedure for axially compressed composite cylinders, Compos. Struct. 93 (12) (2011) 3140–3149, https://doi.org/10.1016/j.compstruct.2011.06.017.
[42] C. Schillo, B. Kriegesmann, D. Krause, Reliability based calibration of safety factors for unstiffened cylindrical composite shells, Compos. Struct. 168 (2017) 798–812, https://doi.org/10.1016/j.compstruct.2017.02.082.
[43] G. Campoli, M. Borleffs, S.A. Yavari, R. Wauthle, H. Weinans, A. Zadpoor, Mechanical properties of open-cell metallic biomaterials manufactured using additive manufacturing, Materials & Design 49 (2013) 957–965, https://doi.org/10.1016/j.matdes.2013.01.071.
[44] M.R. Karamooz Ravari, M. Kadkhodaei, A computationally efficient modeling approach for predicting mechanical behavior of cellular lattice structures, J. Mater. Eng. Perform. 24 (2015) 245–252, https://doi.org/10.1007/s11665-014-1281-4.
[45] E. Verhulp, B. van Rietbergen, R. Müller, R. Huiskes, Indirect determination of trabecular bone effective tissue failure properties using micro-finite element simulations, J. Biomech. 41 (7) (2008) 1479–1485, https://doi.org/10.1016/j.jbiomech.2008.02.032.
[46] B. Lozanovski, D. Downing, P. Tran, D. Shidid, M. Qian, P. Choong, M. Brandt, M. Leary, A monte carlo simulation-based approach to realistic modelling of additively manufactured lattice structures, Additive Manufacturing 32 (2020) 101092, https://doi.org/10.1016/j.addma.2020.101092.
[47] M. Smith, Z. Guan, W. Cantwell, Finite element modelling of the compressive response of lattice structures manufactured using the selective laser melting technique, Int. J. Mech. Sci. 67 (2013) 28–41, https://doi.org/10.1016/j.ijmecsci.2012.12.004.
[48] D. Asprone, F. Auricchio, C. Menna, S. Morganti, A. Prota, A. Reali, Statistical finite element analysis of the buckling behavior of honeycomb structures, Compos. Struct. 105 (2013) 240–255, https://doi.org/10.1016/j.compstruct.2013.05.014.
[49] M. Geißendörfer, A. Liebscher, C. Proppe, C. Redenbach, D. Schwarzer, Stochastic multiscale modeling of metal foams, Probab. Eng. Mech. 37 (2014) 132–137, https://doi.org/10.1016/j.probengmech.2014.06.006.
[50] L. Ning, T. Wilson H, Z. Jiashou, Reliability of elasto-plastic structure using finite element method, Acta. Mech. Sin. 18 (1) (2002) 66–81, https://doi.org/10.1007/BF02487525.
[51] P.L. Clouston, F. Lam, A stochastic plasticity approach to strength modeling of strand-based wood composites, Compos. Sci. Technol. 62 (10–11) (2002) 1381–1395, https://doi.org/10.1016/S0266-3538(02)00086-6.
[52] German Institut for Standardization, Plastics – determination of tensile properties – part 2: Test conditions for moulding and extrusion plastics (ISO 527–2:2012) (2012).
[53] German Institut for Standardization, Plastics - determination of compressive properties (ISO 604:2002) (2003).
[54] ASTM International, Standard test methods for plane-strain fracture toughness and strain energy release rate of plastic materials (2014).
[55] E.W. Andrews, G. Gioux, P. Onck, L.J. Gibson, Size effects in ductile cellular solids. part ii: experimental results, Int. J. Mech. Sci. 43 (3) (2001) 701–713, https://doi.org/10.1016/S0020-7403(00)00043-6.
[56] S. Drücker, S. Inman, B. Fiedler, Simulation and optimization of the load introduction geometry of additively manufactured lattice structure specimens, in: ECCM 2018 - 18th European Conference on Composite Materials, 2018, pp. 1–8.
[57] Z. Zguris, How mechanical properties of stereolithography 3D prints are affected by UV curing (2016).
[58] German Institut for Standardization, Plastics – determination of tensile properties – part 1: General principles (ISO 527-1:2012) (2012).
[59] Dassault Systèmes Simulia Corp., Abaqus 6.14 analysis user's guide (2014).
[60] E. Vanmarcke, Random Fields: Analysis and Synthesis, World Scientific, 2010. doi:10.1142/5807.
[61] W.K. Härdle, L. Simar, Applied Multivariate Statistical Analysis, Springer-Verlag, 2015. doi:10.1007/978-3-662-45171-7.
[62] G. Matheron, Principles of geostatistics, Econ. Geol. 58 (8) (1963) 1246–1266, https://doi.org/10.2113/gsecongeo.58.8.1246.
[63] N.A.C. Cressie, Statistics for Spatial Data, John Wiley & Sons, 1993. doi:10.1002/9781119115151.
[64] T.M. Burgess, R. Webster, Optimal interpolation and isarithmic mapping of soil properties: I the semi-variogram and punctual kriging, J. Soil Sci. 31 (2) (1980) 315–331, https://doi.org/10.1111/j.1365-2389.1980.tb02084.x.
[65] M. Mälicke, H.D. Schneider, Scikit-gstat 0.2.6: A scipy flavoured geostatistical analysis toolbox written in python (2019). doi:10.5281/zenodo.3531816.
[66] W. Weibull, A statistical theory of the strength of materials, Proceedings of the Royal Swedish Institute for Engineering Research 151.
[67] W.V. Liebig, C. Leopold, T. Hobbiebrunken, B. Fiedler, New test approach to determine the transverse tensile strength of CFRP with regard to the size effect, Compos. Commun. 1 (2016) 54–59, https://doi.org/10.1016/j.coco.2016.09.003.
[68] W. Weibull, Zur Abhängigkeit der Festigkeit von der Probengröße, Ingenieur-Archiv 28 (1) (1959) 360–362, https://doi.org/10.1007/BF00536130.
[69] D.C. Drucker, W. Prager, Soil mechanics and plastic analysis or limit design, Q. Appl. Math. 10 (2) (1952) 157–165, https://doi.org/10.1090/qam/48291.
[70] D. Drucker, Plasticity theory strength-differential (SD) phenomenon, and volume expansion in metals and plastics, Metall. Trans. 4 (3) (1973) 667–673, https://doi.org/10.1007/BF02643073.
[71] X.P. Morelle, J. Chevalier, C. Bailly, T. Pardoen, F. Lani, Mechanical characterization and modeling of the deformation and failure of the highly crosslinked RTM6 epoxy resin, Mechanics of Time-Dependent Materials 21 (3) (2017) 419–454, https://doi.org/10.1007/s11043-016-9336-6.
[72] J. Chevalier, P.P. Camanho, F. Lani, T. Pardoen, Multi-scale characterization and modelling of the transverse compression response of unidirectional carbon fiber reinforced epoxy, Compos. Struct. 209 (2019) 160–176, https://doi.org/10.1016/j.compstruct.2018.10.076.
[73] C. Decker, Kinetic study and new applications of UV radiation curing, Macromol. Rapid Commun. 23 (18) (2002) 1067–1093, https://doi.org/10.1002/marc.200290014.
[74] J.G. Kloosterboer, Network formation by chain crosslinking photopolymerization and its applications in electronics, Electron. Appl. (1988) 1–61, https://doi.org/10.1007/BFb0025902.
[75] R. Gümrük, R. Mines, S. Karadeniz, Static mechanical behaviours of stainless steel micro-lattice structures under different loading conditions, Mater. Sci. Eng.: A 586 (2013) 392–406, https://doi.org/10.1016/j.msea.2013.07.070.
[76] H. Alsalla, L. Hao, C. Smith, Fracture toughness and tensile strength of 316L stainless steel cellular lattice structures manufactured using the selective laser melting technique, Materials Science and Engineering: A 669 (2016) 1–6, https://doi.org/10.1016/j.msea.2016.05.075.